Cretaceous Research 173 (2025) 106133

Contents lists available at ScienceDirect

Cretaceous Research

journal homepage: www.elsevier.com/locate/CretRes

Paleoenvironmental changes in the western Tethys carbonate platforms during OAE-2: Implications from phosphorus, $\delta^{18}O$, $\delta^{13}C$ and facies analysis

Sahara Cardelli [a], Barbora Křížová [a, b], Michele Morsilli [a], Renato Posenato [a], Thierry Adatte [c], Brahimsamba Bomou [c], Jorge E. Spangenberg [d], Lorenzo Consorti [e], Amerigo Corradetti [b], Marco Franceschi [b], Valentina Brombin [a], Gianluca Frijia [a, *]

[a] Dipartimento di Fisica e Scienza della Terra, Università di Ferrara, Ferrara, Italy
[b] Dipartimento di Matematica, Informatica e Geoscienze, Università degli Studi di Trieste, Trieste, Italy
[c] Institute of Earth Sciences, University of Lausanne, Lausanne, Switzerland
[d] Institute of Earth Surface Dynamics, University of Lausanne, Lausanne, Switzerland
[e] Istituto di Scienze Marine, Consiglio Nazionale delle Ricerche (ISMAR-CNR), Trieste, Italy

ARTICLE INFO

Article history:
Received 6 June 2024
Received in revised form
16 March 2025
Accepted in revised form 21 March 2025
Available online 1 April 2025

Keywords:
OAE-2
Carbonate platforms
P concentrations
Biota evolution
Paleotemperature changes
Paleoenvironmental changes

ABSTRACT

Oceanic anoxic event 2 (OAE-2) is one of the largest paleoclimatic events of the whole Phanerozoic which occurred at the Cenomanian/Turonian Boundary (CTB). It caused major perturbation of the C-cycle at global scale together with changes in other geochemical cycles. OAE-2 severely impacted marine and terrestrial settings causing faunal turnovers both in pelagic and neritic environments. The exact mechanisms triggering OAE-2 are debated but it is believed that the main driver was a massive injections of volcanic CO_2 in the atmosphere. The effect of OAE-2 on deep-water communities has been extensively documented in literature. In contrast, less data are available for their shallow-waters counterparts. Geochemical and semiquantitative facies analysis on samples from two carbonate platforms located in Italy (former western Tethys) are presented in this paper, where new data from the Friuli-Adriatic Carbonate Platform are compared with a well-known section from the Apennine Carbonate Platform. Our data show a good correlation between these platforms, located 1000 km apart. Phosphorus concentrations are low except for two intervals: (1) at the onset of the OAE-2 and (2) in the late phase of the event. The $\delta^{18}O$ record shows an increase of the Sea Surface Temperature (SST) during the event interrupted by a cooler interval. Our data indicate a correlation between geochemical changes and faunal turnover of benthic foraminifera and rudists, suggesting the co-occurrences of several causes for the demise of these groups during OAE-2.
© 2025 The Author(s). Published by Elsevier Ltd. This is an open access article under the CC BY license (http://creativecommons.org/licenses/by/4.0/).

1. Introduction

The Late Cretaceous super-greenhouse period (Steuber et al., 2005; Takashima et al., 2006) witnessed one of the most significant paleoceanographic and paleoclimatic events of Earth's history: the Oceanic Anoxic Event 2 (OAE-2, Bonarelli Event). This occurred at the Cenomanian/Turonian boundary (CTB, ca. 94 Ma) and represents one of the largest short-term (~430–930 kyr) perturbations of the global carbon cycle in the stratigraphic record (Gangl et al., 2019). OAE-2 was due to a sharp rise of paleotemperatures that culminated in the highest values of the whole Cretaceous during the early Turonian (O'Brien et al., 2017).

Global warming led to an acceleration of the hydrological cycle, enhanced continental weathering, and increased input of nutrients into the oceans, which resulted in high primary productivity and the development of anoxic conditions in many oceanic basins around the world (e.g. Snow et al., 2005; Jenkyns 2010; Owen-Smith et al., 2017; Clarkson et al., 2018). The proposed main trigger mechanism for the onset of OAE-2 was increased levels of greenhouse gases in the atmosphere-ocean system related to high volcanic activity of mid-ocean ridges (Larson 1991; Seton et al., 2009) and/or volcanic outgassing associated with the emplacement

* Corresponding author.
E-mail address: gianluca.frijia@unife.it (G. Frijia).

https://doi.org/10.1016/j.cretres.2025.106133
0195-6671/© 2025 The Author(s). Published by Elsevier Ltd. This is an open access article under the CC BY license (http://creativecommons.org/licenses/by/4.0/).

of Large Igneous Provinces (LIPs) (Larson 1991; Jones and Jenkyns 2001; Du Vivier et al., 2015). Sedimentologically, the most characteristic expression of OAE-2 is the deposition of organic carbon-rich levels (black shales), at global scale (Schlanger and Jenkyns 1976; Takashima et al., 2006; Jarvis et al., 2011).

The deposition and preservation of high amounts of organic matter caused a global positive shift of $\delta^{13}C$ values (2–4 ‰) of organic and inorganic carbon, in both marine and terrestrial sediments (e.g. Scholle and Arthur 1980; Tsikos et al., 2004; Jarvis et al., 2011). This large Carbon Isotope Excursion (CIE) is the key chemostratigraphic characteristic of the OAE-2 (e.g. Tsikos et al., 2004; Kraal et al., 2010). The OAE-2 CIE presents a distinct pattern composed of two positive peaks, a trough, and a plateau phase before the $\delta^{13}C$ values return to their pre-event values (e.g., Paul et al., 1999; Jarvis et al., 2011). This pattern is clearly identifiable in reference curves of the OAE-2 carbon isotope fluctuations derived from hemipelagic and pelagic sedimentary successions. Nonetheless, in recent years, an increasing number of studies have reproduced the complex pattern of OAE-2 CIEs also in shallow–water successions, where similar excursions have been confirmed (Parente et al., 2007, 2008; Korbar et al., 2012; Frijia et al., 2015, 2019; Bomou et al., 2020). These findings allowed high-resolution comparison between deep-water and shallow-water areas, and enhanced the understanding of the response of neritic areas to oceanic perturbations.

A complex interplay between variations in nutrients supply, the spread of anoxia in many oceanic basins, eustatic sea level and temperature fluctuations, as well as modification of several geochemical cycles, affected the carbonate platform production during the OAE-2 (Steuber et al., 2023 and reference therein; Křížová et al., 2024). This resulted in many carbonate platforms drowning during the late Cenomanian (e.g. Drzewiecki and Simo 1997; Brčić et al., 2017), or preserving a continuous shallow-water record across the CTB interval. These resilient platforms, however, were severely impacted by OAE-2, with major faunal turnovers among their benthic communities (Parente et al., 2008; Navarro-Ramirez et al., 2017; Frijia et al., 2019; Bomou et al., 2020; Steuber et al., 2023; Křížová et al., 2024).

Despite evidence of the profound impacts of OAE-2 on carbonate platforms evolution, the causes and trigger mechanisms and their link to the observed paleoenvironmental changes are yet to be fully understood. A recent study suggests that temperature changes might have been the major factor responsible for the faunal turnover of larger benthic foraminifera and rudists at the CTB (Křížová et al., 2024). Nevertheless, significant uncertainty still exists with regard to the impact of other factors, such as anoxia, sea-level fluctuations, geochemical variations and overall nutrient supply (see Steuber et al., 2023; Petrizzo et al., 2025 for a review).

This study aims to clarify the interplay between increase in temperature and other factors, by reporting a detailed investigation of three shallow carbonate stratigraphic sections cropping out in the Friuli-Adriatic Carbonate Platform and the Apennine Carbonate Platform of Italy, where a continuous record of the OAE-2 in shallow–water carbonates is preserved (Parente et al., 2008; Jenkyns 2010; Owens et al., 2013; Clarkson et al., 2018; Frijia et al., 2019; Křížová et al., 2024).

Several geochemical proxies (P, $\delta^{18}O$, $\delta^{13}C_{carb}$, $\delta^{13}C_{org}$, TOC) have been used to understand nutrient cycling, as well as organic matter accumulation and preservation. In particular, for the first time, phosphorus (P) measurements are presented for the carbonate platforms of the Tethyan realm. Phosphorus, is considered a proxy for primary productivity and P concentration data have been used to shed significant insights into the nutrient cycling during the OAE-2 event (Mort et al., 2007). Despite their relevance, the P records across the entire OAE-2 are rather limited and mostly derived from deep water deposits (Mort et al., 2007; Gertsch et al., 2010; Kraal et al., 2010; Westermann et al., 2010; Bomou et al., 2013). To date, P cycling in shallow–water carbonates has been addressed only by one study from the Mexico Platform (Bomou et al., 2020) and this lack of data hampers a full understanding of nutrient cycling during OAE-2 (Kraal et al., 2010). Finally, we complete the dataset with a comprehensive sedimentological and paleontological characterization of the studied sections to enhance understanding of the paleoenvironmental impact of OAE-2 on the shallow-water carbonate platforms of western Tethys.

2. Geological setting

The Cretaceous peri-Mediterranean area was largely characterized by an articulated system of isolated carbonate platforms separated by pelagic and hemipelagic basins (Vlahović et al., 2005; Patacca and Scandone, 2007), with a low-energy inner platform setting predominating, rare high-energy shoals, and subtidal areas characterised by larger foraminifera and rudists (Parente et al., 2008; Frijia et al., 2015).

The Friuli-Adriatic Carbonate Platform (hereafter, FCP) represented the northernmost margin of the larger Adriatic Carbonate Platform (AdCP). The latter was one of the largest Mesozoic carbonate platforms of the peri-Mediterranean region, which developed on the proximal passive margin of the Adria microplate from the Late Triassic, extending across contemporary western Balkans to northeastern Italy (Vlahović et al., 2005; Picotti and Cobianchi, 2017; Picotti et al., 2019; Consorti et al., 2021). The FCP was a persistent shallow-water domain during the Cretaceous with a major episode of major subaerial exposure suggested by the presence of paleokarst features in the latest Cretaceous to Paleocene. The platform was bounded by the Belluno and Tolmin-Slovenian basins (Fig. 1B, see Křížová et al., 2024 for a detailed geological description).

Lithostratigraphically, the intervals investigated for this research (Fig. 1C) belong to the “Aurisina limestone” unit (upper Cenomanian to lower Campanian), which consists of facies deposited in a low-energy inner platform setting. The “Aurisina limestone” is mainly composed of peritidal cycles consisting of alternating thick layers of rudist floatstones and thin layers of wackestone with cyanobacteria (*Decastronema* spp.), algae (*Thaumatoporella* spp.) and benthic foraminifera. The most notable feature of the lower part of the “Aurisina limestone”, observed in the field, is the occurrence of large bivalves like *Chondrodonta* and rudists (Posenato et al., 2020; Del Viscio et al., 2022; Křížová et al., 2024). Locally the basal part of the “Aurisina limestone” contains the so-called “Zolla member” (Fig. 1C). The latter is composed of bivalve (rudists and *Chondrodonta*) -foraminiferal floatstone associated with, or intercalated to, dolomitized and laminated dark grey, organic-rich wackestones, often containing the pelagic algal taxon *Pithonella*. Around the CTB, a temporary platform drowning was recorded over a major part of the AdCP, possibly related to the interplay of local factors and global perturbations associated with OAE-2. This drowning caused the disappearance of numerous shallow-water benthic invertebrate taxa and the occurrence of planktonic organisms, including calcispheres (Vlahović et al., 2005; Korbar et al., 2012; Brčić et al., 2021). Nonetheless, recent data (Křížová et al., 2024) indicate that the Friuli sector of the AdCP, although severely affected by the OAE-2, did not drown and preserved an almost continuous record of shallow–water facies during OAE-2.

For this study, two areas situated around 50 km apart were analyzed: Monrupino and Devetachi. The first of these (MR; 45.71613° N, 13.81028° E) is located 11 km northeast of Trieste (Trieste Karst area) (Fig. 1D) and comprises a 95 m-thick composite

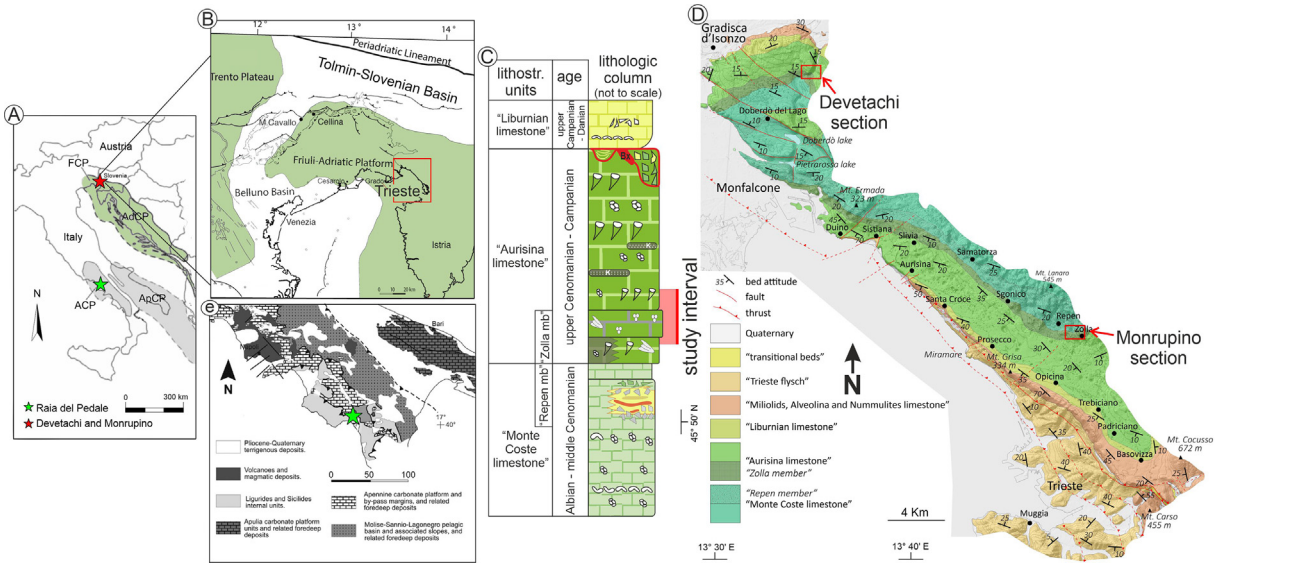

Fig. 1. (A) Present day distribution of Adriatic and Apennine carbonate platform deposits (AdCP and ACP respectively) from Vlahovich et al., (2005). The red star indicates the position of the two sections studied in the Friuli sector of the AdCP (Devetachi and Monrupino, in the Friuli Carbonate Platform FCP) and the green star the location of the section in the ACP (Raia del Pedale). (B) Cretaceous paleogeographic map (after Picotti et al., 2019) of the Friuli Carbonate Platform (FCP); (C) Simplified lithostratigraphic units of the northwestern part of the Adriatic Carbonate Platform from Consorti et al. (2021). (D) Geological map of the Italian Karst (simplified from Jurkovšek et al., 2016). (E) Simplified geological map of southern Apennines (from Parente et al., 2007). The position of the studied Raia del Pedale section is indicated by the green star.

section of Cenomanian–Turonian shallow-water carbonates; the second section (DEV; 45.86878° N, 13.57274° E) is located close to the Italian–Slovenian border and crops out in the so-called Gorizia Karst area (Fig. 1D). This stratigraphic section has been studied in detail by Křížová et al. (2024) and consists of 144.4 m of upper Cenomanian–middle Turonian shallow–water carbonates. Here, only the first 70 m encompassing the OAE-2 interval are considered.

The two Friuli carbonate successions from north-east Italy were compared to the reference OAE-2 shallow–water section of Raia del Pedale (RdP - southern Italy; Fig. 1A, E; Parente et al., 2008; Clarkson et al., 2018; Frijia et al., 2019), belonging to the Apennine Carbonate Platform (ACP). This paleogeographic unit consists of a thick pile of Mesozoic carbonates deposited in shallow tropical waters at the southwestern margin of the Neo-Tethys Ocean (Frijia et al., 2015 for details on the geological evolution of the ACP).

3. Material and methods

This study was carried out through a multidisciplinary approach, integrating the datasets of Křížová et al. (2024) for the Devetachi section (FCP), and of Frijia et al. (2019) and Parente et al. (2008) for the Raia del Pedale section (ACP). All data from the Monrupino section (FCP) are presented for the first time in this study, while the facies analysis descriptions, carbon and oxygen data from Devetachi, as well as most geochemical analyses ($\delta^{13}C$, $\delta^{18}O$, $\delta^{13}C_{org}$, TOC) from Raia del Pedale (ACP) have been published in previous studies (Frijia et al., 2019; Křížová et al., 2024). Tables with all the new geochemical data (bulk rock and shells) are provided as "Supplementary Material". The presented dataset consists of: (1) facies and micropaleontological analyses; (2) carbon and oxygen stable isotope values of bulk samples and shells; (3) organic carbon isotopes analyses; (4) TOC contents derived by Rock-Eval Pyrolysis; (5) P concentration data. Samples and thin section material (coded DSS, SD, REP and EM) are stored at University of Ferrara. Except for stable isotope analyses of carbonate and organic carbon (C_{carb}, C_{org}) and oxygen, all samples were previously reduced to powder in two steps. The rock slabs of several cm were first crushed into pieces no bigger than 5 mm by a jaw crusher *Fritsch "Pulviresette 1"*, and finely powdered by a mortar mill Model *"MG 100" Laarmann*, with an agate grinding set.

3.1. Fieldwork and thin-section microscopy

The stratigraphic sections of Devetachi and Monrupino were sampled at decimeter - to-meter intervals. A higher centimetric resolution sampling was applied across particular intervals. In total, 265 samples were collected and 90 thin sections were prepared for petrographic and micropaleontological analyses. Thin sections were used for diagenetic observations, and to select the most suitable samples for geochemical analyses. Sample composition for facies analysis was semi-quantitative and is reported in terms of relative abundance.

3.2. Determination of $\delta^{13}C_{carb}$ and $\delta^{18}O$

The stable isotopes composition of 141 samples of bulk rock and 64 samples of well-preserved rudist and *Chondrodonta* shells were determined from the Monrupino section. About 2–3 mg of powder was obtained for each sample by micro-drilling a polished rock slab under a binocular microscope. Polished thin sections were analyzed to identify areas free of bioclasts and/or evidence of recrystallization. The micro-sampling was performed using drill bits of different diameters: 0.8 mm for lime mudstones, 0.5 mm for the micritic matrix of granular bioclastic facies, and 0.3 mm for the shells. Stable isotope analyses were carried out at the University of Ferrara (Italy) using *isoFLOW* (Elementar©) and a *PrecisION* IRMS (Elementar©) in continuous flow. The results are reported as δ values relative to the VPDB standard. Precision (1σ), monitored by repeated analyses of international and laboratory standards, was ±0.1 ‰ for carbon and oxygen. Replicate measurements gave reproducibility in the range of ±0.1 ‰ for $\delta^{13}C_{carb}$ and ±0.2 ‰ for $\delta^{18}O$. All samples (irrespective of their absolute isotopic values) with macro- and micro-evidence of subaerial exposure/dissolution features were not plotted in the isotopic profiles, following the approach of Del Viscio et al. (2022) and Křížová et al. (2024). Nineteen bivalve shell samples from the

Raia del Pedale section were measured for $\delta^{18}O$, using the same shells used in Frijia et al. (2019) to build the $\delta^{13}C$ shell curve throughout OAE-2. In all sections, where different shell fragments were analysed for single beds, average $\delta^{13}C_{carb}$ and $\delta^{18}O$ values were calculated in order to minimize the effects of diagenesis and/or shell ontogenic isotopic variability.

3.3. Determination of organic $\delta^{13}C$

Organic $\delta^{13}C$ ($\delta^{13}C_{org}$) analyses were conducted on 37 samples from the Devetachi section following same procedure described by Khozyem et al. (2021). Two to 4 g of powders were weighed into 50 ml Falcon™ vials and reacted with 1.2 M HCl acid at room temperature until the carbonate portion was completely dissolved. After this, the tubes were centrifuged using a Bench Top Centrifuge NEYA 8 XS, to concentrate the residue, which was rinsed with deionized water (Milli-Q) at least 3 times, until a neutral pH was reached, and dried in an oven at 40 °C (~16 h). After drying, the insoluble residue samples were regrounded and submitted to organic carbon isotope analysis by flash combustion on a *Carlo Erba 1108* elemental analyzer (EA) connected to a *Thermo Fisher Scientific Delta S* isotope ratio mass spectrometer (IRMS), operating in the continuous helium flow mode via a *Conflo III* split interface (EA–IRMS). Organic carbon isotope analyses were performed at the Institute of Earth Sciences of the University of Lausanne (UNIL, Switzerland). The $\delta^{13}C_{org}$ values are reported relative to VPDB. The calibration and assessment of the reproducibility and accuracy of the isotopic analysis were based on replicate analyses of laboratory standard materials and international reference materials. The reproducibility was better than 0.1 ‰ $\delta^{13}C_{org}$ (1σ).

3.4. Determination of total organic carbon (TOC)

A total of 69 dry powdered whole rock samples from the Devetachi section were analyzed using a *Rock-Eval 6 pyrolyzer* (*Vinci Technologies*) at the Institute of Earth Sciences, University of Lausanne, Switzerland. Following the procedure outlined by Percival et al. (2015), approximately 65–80 mg of each sample (depending on whether the sample was more carbonate- or organic matter-rich, a distinction made based on color) were measured into gauze crucibles, and their precise mass was determined. A carousel was loaded with fifty crucibles. The samples were placed in an oven and initially heated at 300 °C under an inert atmosphere, gradually pyrolyzed up to 650 °C (heating rate of 25 °C/min). After this first step, the samples were transferred into another oven and gradually heated up to 850 °C in the presence of air. The resulting CO and CO_2 were analyzed spectrally.

The Rock-Eval 6 results include total organic carbon content (TOC, wt.%), hydrogen index (HI, mg HC/g TOC, HC = hydrocarbons), oxygen index (OI, mg CO_2/g TOC), and T_{max} values (°C, OM thermal maturity indicator, the temperature at which maximum cracking of kerogen in a sample occurs). The HI and OI parameters are used to distinguish between algal/bacterial (type I and II kerogens) and terrestrial and/or reworked (type III and IV) OM. HI (in mg HC g^{-1} TOC) corresponds to the amount of HC released relative to TOC. OI (in mg O2 g^{-1} TOC) corresponds to the amount of oxygen released as CO and CO_2, relative to TOC. The T_{max}, OI, and HI parameters were only interpreted for TOC values $\geq$ 0.25 wt% (Espitalié et al., 1985). Samples were calibrated using the IFP160000 standard with an instrumental precision of 2 % (Espitalié et al., 1985; Percival et al., 2015; Khozyem et al., 2021).

3.5. Determination of total phosphorus (P)

Total phosphorus analyses were performed for the Devetachi (n = 42) and Raia del Pedale (n = 56) sections, and were conducted at the University of Lausanne using the ascorbic acid molybdate blue method (Eaton et al., 1996). About 100 mg (±5 mg) of powdered sample were weighed and placed in decontaminated glass bottles covered with aluminum foil for ventilation. A 0.5 ml solution of magnesium nitrate (1 M) was added to degrade organic matter. After drying at 100 °C, the bottles underwent ashing in a furnace at 550 °C for 2 h and 30 min. Subsequently, 10 ml of HCl (1 M) was introduced, and the bottles were placed in an ultrasonic bath for sample disaggregation to release phosphorus from the sediment matrix. The samples were then filtered and diluted tenfold. A solution containing 90 µl of molybdate mixing reagent and ascorbic acid was added to 3 ml of the solution. The intensity of the blue color, correlating with phosphorus concentration, was measured with an ultraviolet-visible (UV/Vis) *PerkinElmer Lambda 25* spectrophotometer. The concentration of PO_4 (in mg/L) was obtained by calibration with internal standard solutions with a precision better than 5 %. In this study we chose to determine total P (P_{tot}) instead of sedimentary P fractions, as it likely more robustly reflects phosphorus dynamics in ancient marine settings (Gertsch et al., 2010; Bomou et al., 2013, 2020). In order to overcome possible bias on total P content imposed by changes in facies/sedimentation rates in the studied sections, P mass-accumulation rates (P MAR-mg/cm^2/kyr) were calculated using the equation reported by Bomou et al. (2013). Evaluation of the sedimentation rates in both the Raia and Devetachi sections were estimated via carbon-isotope correlations of the OAE-2 intervals (onset to peak a, peak a to peak b, peak b to the end of OAE-2) in the studied sections with the Late Cretaceous $\delta^{13}C$ reference curve of Cramer and Jarvis (2020). Due to the lack of time constrains below and above the OAE-2 interval in both sections we chose a more conservative sedimentation rate for these intervals which was considered smaller than the minimum obtained through OAE-2. A rock density of 2.5 g/cm3 was used for pure limestone and for the laminite facies (slightly argillaceous) following Bomou et al. (2013).

4. Results

4.1. Friuli Carbonate Platform: facies analyses and geochemistry

The two studied sections of the FCP exhibit a similar facies evolution, both consisting of inner platform limestones where peritidal cycles dominate. Evidence of short-lasting emersion episodes is quite frequent, occurring mainly in their lower and upper parts. Dominant skeletal components are larger foraminifera and molluscs (mainly rudists). *Chondrodonta* are quite abundant in the upper Cenomanian interval.

Implementing the data from Křížová et al. (2024) with the new analyses performed in this study, fifteen lithofacies were identified in the FCP across the CTB based on texture, grain types, and sedimentary structures. These lithofacies have been grouped into 4 lithofacies associations and interpreted in terms of depositional environment (Table 1, Fig. 2). The benthic fauna includes mainly bivalves (rudists and *Chondrodonta*), benthic foraminifera, dasycladales, and micro encrusters problematica. A complete description of the facies evolution and geochemistry of the two sections from the FCP is reported below.

Table 1
Lithofacies from the Friuli-Adriatic Carbonate platform with the main characteristics (texture, components, and sedimentary structures), their occurrence in the two studied sections (DEV – Devetachi; MR – Monrupino), lithofacies association (LA), and interpreted depositional environment.

	Lithofacies	Lithofacies description	Occurrence	Lithofacies association and depositional environment
MW	MDST/WKST with micropeloids	MDST/WKST with micropeloids, sparse ostracods, Thaumatoporella and small benthic foraminifera. Sometimes with cement-filled vugs.	DEV	LA 1 Intertidal setting
WV	WKST with vugs	WKST/PKST often with cement-filled vugs and/or rarely fenestrae, peloids, small benthic foraminifera, sometimes intraclasts, and rare Thaumatoporella, ostracods, nubeculariids, cyanobacterial filaments and nodules.	DEV	
LB	Laminated bindstone	Laminated bindstone with intercalation of thin, organic-rich crinkly laminae and micropeloidal-bioclastic laminae.	DEV; MR	
LP	Laminated PKST	Faintly laminated PKST, with micritized intraclasts, small fragments of ostracods and bivalve shells, in place residual organic matter.	MR	
PP	PKST with peloids	PKST with peloids, fragments of bivalves, small benthic foraminifera, ostracods and Thaumatoporella.	DEV; MR	LA 2 Intertidal to shallow subtidal setting
BG	Bioclastic GRST with peloids	Bioclastic GRST with bivalve shell fragments (rudists and Chondrodonta), often peloids. Sometimes few small benthic foraminifera and echinoderm fragments.	DEV; MR	
WF	WKST/PKST with larger foraminifera	WKST/PKST with large and high diversity benthic foraminifera, peloids, moderate fragmented bivalve shells, ostracods and Thaumatoporella.	DEV	LA 3 Shallow water inner platform setting with low to moderate water energy
GP	PKST/FLST with gastropods fragments and intraclasts	PKST/FLST, occasionally GRST, with large gastropods, intraclasts, bivalve fragments (usually rudists), peloids and fragments of green algae.	DEV; MR	
WP	WKST/PKST with thin rudist fragments	WKST/PKST with small, thin rudist fragments, rare benthic foraminifera, ostracods, and rare gastropods. Micritized intraclasts are common and dascycladaceans present in few beds.	DEV	
DW	Microbioclastic WKST/PKST, often dolomitized	Microbioclastic-micropeloidal PKST, partially dolomitized, rudist and indeterm. recrystallized bivalve fragments, echinoderm fragments, sometimes benthic foraminifera. Rare ostracods and rare calcispheres or sponge spicules.	MR	
MP	Microbioclastic PKST	Microbioclastic PKST with highly fragmented indeterm. bivalve shells, echinoderm fragments, often micropeloids, present rotalids. Sometimes also rare corals and small gastropods, in place with calcisphere.	DEV; MR	LA 4 Moderate to high water energy open subtidal setting, with tidal channels
BP	Bivalve PKST	Bioclastic PKST with highly fragmented rudist bivalve shells, Chondrodonta and ostreid shells and echinoderms fragments, often peloids.	DEV; MR	
RP	Rudist PKST/FLST	Rudist PKST with highly fragmented, thin-elongated rudist and subordinated Chondrodonta shell fragments.	DEV; MR	
RF	Rudist FLST	FLST/RDST with large Rudist shells and fragments. Sometimes intraclasts and peloids are also present, and rare benthic foraminifera.	DEV; MR	
CH	Chondrodonta FLST/RDST	FLST/RDST with Chondrodonta and subordinated rudist shells.	DEV; MR	

4.1.1. Monrupino section

The facies evolution in the Monrupino section shares strong similarities with the Devetachi section except for having a poorer benthic foraminiferal content. For comparison with Devetachi, the succession was divided into four stratigraphic intervals (1–4, Fig. 3).

Interval 1 (0–31 m): the base is characterized by 7 m of thick beds (ranging from 80 cm to 3 m) of bioclastic-bivalve packstone (BP) followed by a floatstone with fragmented and whole rudists. Upwards, the section continues with around 14 m of blackish, fetid and partially dolomitized microbioclastic-micropeloidal packstone (DW) with sporadic calcispheres in the last meters. This facies is present only in this section and is likely associated with the so-called "Zolla Member" (see section 2), a lithostratigraphic unit that is laterally discontinuous across the FCP. Alternating with the DW facies, between about 9 and 13 m, centimeter-thick layers of laminated bindstone (LB) are present. The uppermost part of interval 1 is represented by 7 m of packstone with highly fragmented indeterminate bivalve shells packstone (MP). The foraminifera in this interval are quite rare and mainly represented by: *Cuneolina* sp., Discorbidae, Miliolidae, *Neodubrovnikella turonica*, *Rotorbinella mesogeensis*, *Rotorbinella* sp. This assemblage suggests a late Cenomanian age (Chiocchini et al., 2012; Schlagintweit and Yazdi-Moghadam, 2022; Křížová et al., 2024).

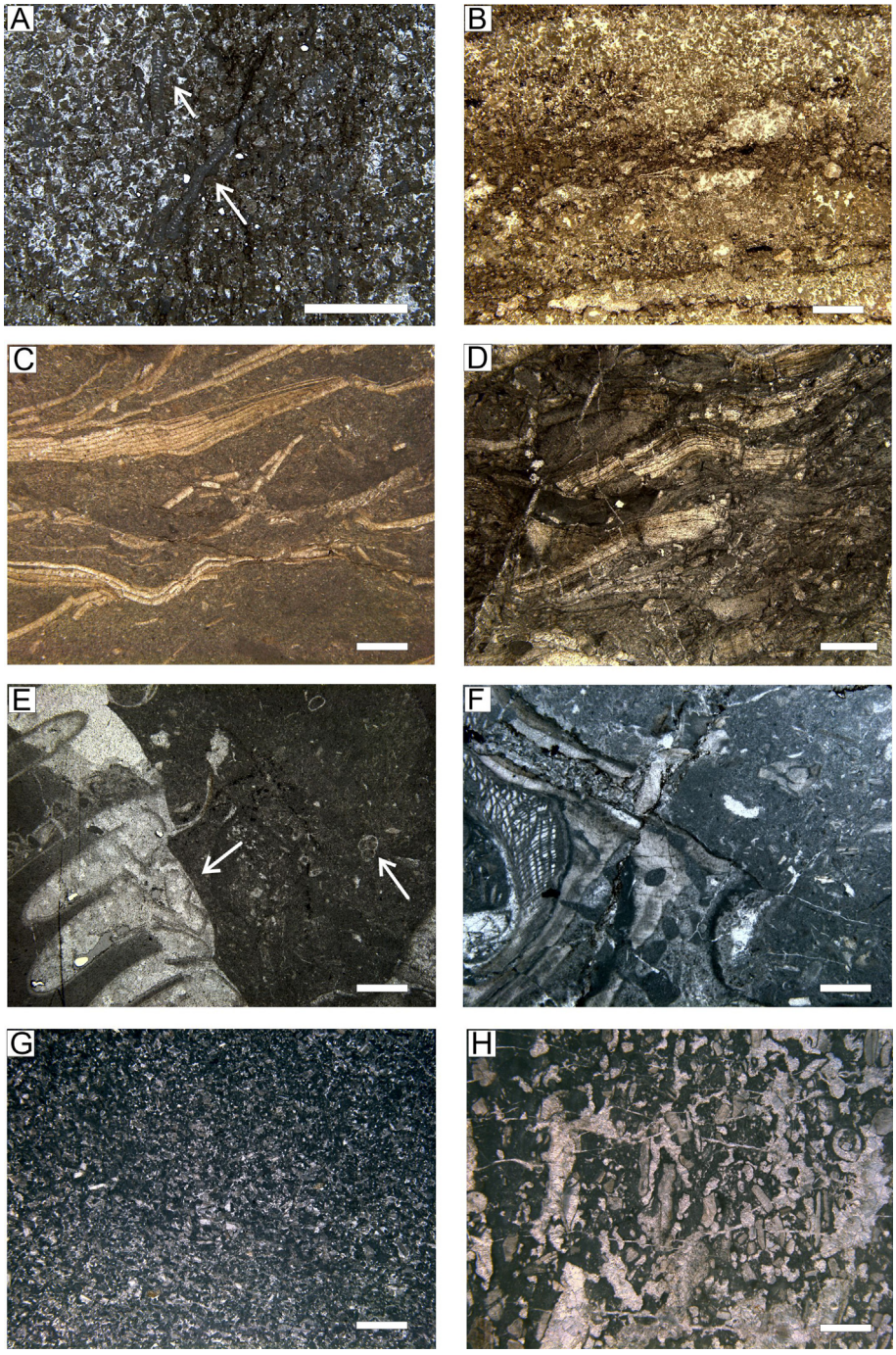

Fig. 2. Representative microfacies of the Cenomanian/Turonian interval of the Friuli Carbonate Platform. (A) Wackestone/packstone with large benthic foraminifera (white arrows indicate *Pastrikella balcanica* specimens)– WF (sample: DSS 1.5; Section: DEV); (B) laminated bindstone– LB (DSS 7-4b; DEV); (C) packstone with highly fragmented, thin elongated rudist shells – RP (EM 28.2; MR); (D) *Chondrodonta* floatstone/rudstone – CH (EM 9.8; MR); (E) packstone/floatstone with gastropods (white arrows) – GP (SD 10.9; DEV); (F) Rudist floatstone – RF (REP 51.4; MR); (G) peloidal packstone – PP (REP 38.5; MR); (H) wackestone/packstone with cement-filled vugs and/or fenestrae – WV (REP 71.2; MR). The scale bar is 2 mm for all the photographs.

Interval 2 (31–66 m) begins with a regular alternation of centimeter-thick layers of bioclastic bivalve packstone (BP) and *Chondrodonta* floatstone (CH), capped by 10 m of packstone–floatstone with thin elongated rudist fragments (RP). At the top of interval 2, there are thick meter-scale beds of bioclastic packstone with rudist debris (BP) (Table 1; Fig. 3). No foraminifera are present.

Interval 3 (66–86 m) consists mainly of BP facies alternating with meter-thick beds of rudist floatstone (RF), with the exception, in the middle part, of 3 m of packstone/grainstone with gastropods

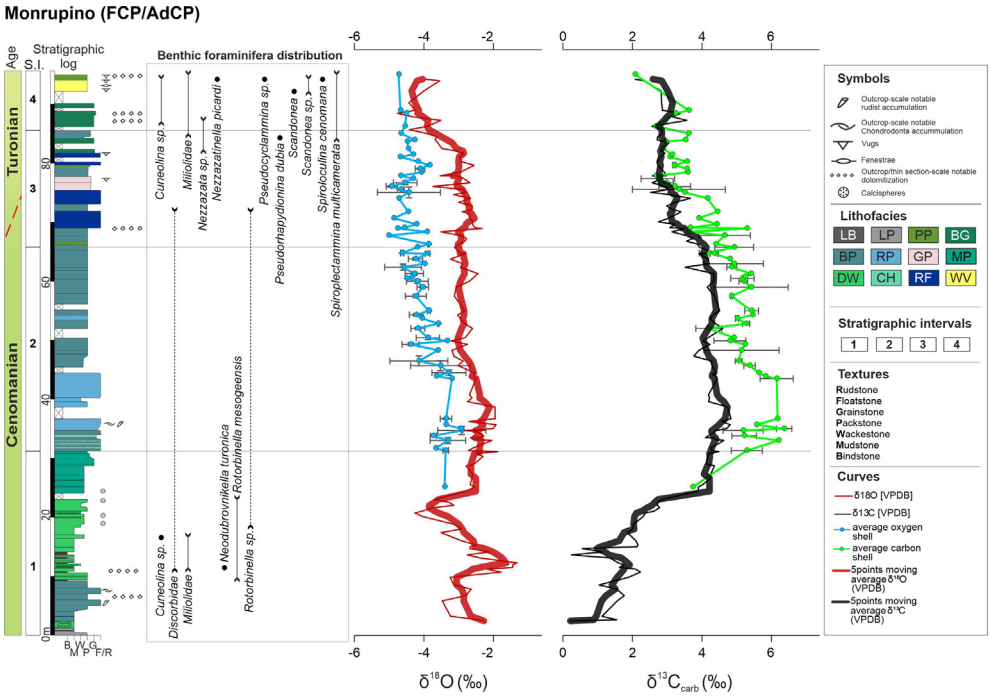

Fig. 3. Monrupino section: lithological – sedimentological log, range of the most significant benthic foraminifera, oxygen- and carbonate carbon-isotope stratigraphy (‰ VPDB) both from bulk rock and shells. The section has been subdivided into four intervals (1–4) based on lithofacies and biostratigraphy. The dashed red line on the chronostratigraphic column indicates the Cenomanian/Turonian boundary defined by biostratigraphic data. VPDB – Vienna Peedee belemnite. Geochemical data available as "Supplementary Material".

(GP). A few, centimetre-thick layers of peloidal packstone (PP) and grainstone with peloids and bivalve shell fragments (BG) are also present in this interval. The foraminiferal fauna in this interval is scarce, except for a single sample in which *Rotorbinella* sp., and Discorbidae were found.

Interval 4 (86–95 m) starts with 4 m of bioclastic grainstone with peloids (BG), followed by 2.4 m-thick beds of wackestone with cement-filled vugs and fenestrae (WV), which passes into a peloidal packstone (PP) towards the top. Dolomitization is quite frequent. The most significant benthic foraminifera are: *Cuneolina* sp., Miliolidae, Nezzazatidae, *Nezzazata* sp., *Scandonea* sp., *Siphopfenderina* sp., *Spiroplectammina multicamerata*. This assemblage suggests a Turonian age according Frijia et al. (2015).

4.1.1.1. Stable isotope data ($\delta^{13}C_{carb}$, $\delta^{18}O$) of bulk micrite and bivalve shells. Closely spaced sampling allowed for the reconstruction of a high-resolution $\delta^{13}C$ and $\delta^{18}O$ record using both bulk-rock and bivalve shell samples (respectively black and green curves for C-isotopes, and red and light blue for O-isotopes, Fig. 3).

One hundred and twenty-eight samples of bulk-rock and 64 of rudist shells were analyzed for the Monrupino section. Unfortunately, the shell record at Monrupino is incomplete due to the absence of well-preserved shell fragments in the lowest 25 m of the section. The $\delta^{13}C$ and $\delta^{18}O$ trends in the bulk rock and the shell material are very similar, with a consistent difference in the absolute values of~ 2 ‰, with the shells having, generally a more positive signature for $\delta^{13}C$. Furthermore, the $\delta^{13}C$ shell values show higher variability compared to the bulk across the same interval (Fig. 3). This pattern is also observed in the Devetachi succession (Křížová et al., 2024; see Fig. 4).

At the base of interval 1, the $\delta^{13}C$ isotope curve exhibits an increasing trend, reaching a first peak of positive values, with a maximum of 4.36 ‰ at ~28 m (Fig. 3). Subsequently, the $\delta^{13}C$ trend shows a minor inflection, which lasts 2 m followed by a subtle increase, culminating in a second maximum $\delta^{13}C$ raw bulk value of 4.83 ‰ around 37m. Here also, the shell curve records the highest value of 6.36 ‰. From this point upwards in interval 2, the $\delta^{13}C$ bulk curve shows a plateau with values of between 3.7 and 4.4 ‰. This trend is mirrored in the shell $\delta^{13}C$ profile, despite the slightly higher values of the rudists' signature (between 4.2 and 5.8 ‰). From the base of interval 3, the carbon isotope profiles (bulk and shells) exhibit a sharp decreasing trend, which becomes stable in interval 4 with values fluctuating around 2 and 2.5 ‰. The $\delta^{18}O$ bulk profile, from the base of the section, shows a general decreasing trend both in the raw bulk and shell components towards the top with values of between −1.3 and −4.7 ‰ (raw bulk) and between −2.9 and −5 ‰ (shells) at the top of the section.

4.1.2. Devetachi section

The upper Cenomanian–lower Turonian of the Devetachi section was subdivided into four intervals (1–4, Fig. 4) by Křížová et al. (2024). Here we report a refined description of the intervals and a more detailed facies characterization based on semiquantitative facies analyses (Fig. 4). For biostratigraphic and chronostratigraphic results the reader is referred to Křížová et al. (2024) and to Fig. 4, where the stratigraphic ranges of the most relevant identified taxa are reported.

Interval 1 (0–20 m) comprises in its lowest 15 m, a coarsening upward trend from microbial bindstone (LB) that evolve upwards into wackestone/packstone with benthic foraminifera (WF) alternating with decimetric beds of peloidal packstone (PP) and bioclastic grainstones (BG). In the top 5 m of interval 1, microbioclastic packstone (MP) and wackestone with thin rudist shells (WP) are present. Between 10 and 20 m from the base of the section, sporadic calcispheres were found, mainly in the microbioclastic packstone (MP) and laminated bindstone (LB) facies. Interval 2 (20–40 m) is characterized by a 5 m thick interval where centimeter-scale layers of bivalve packstone (BP) alternate with *Chondrodonta* floatstone (CH). This is followed upwards by a 10m-thick rudist interval dominated by thin elongated fragments of

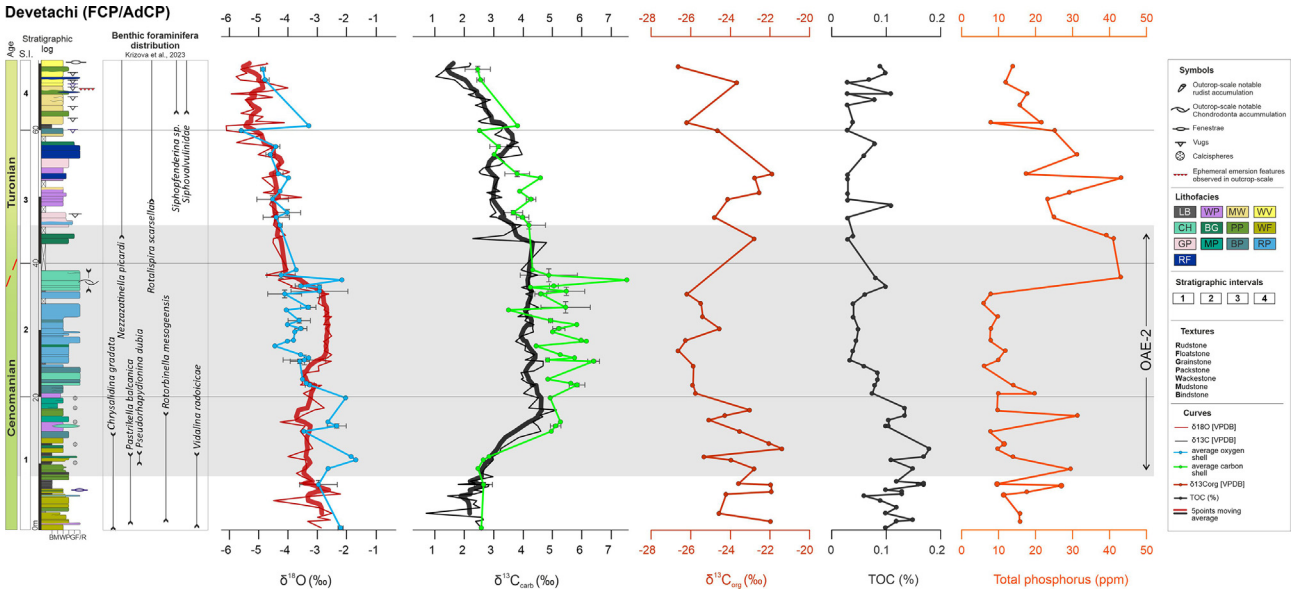

Fig. 4. Devetachi section: lithological – sedimentological log, benthic foraminifera distribution; oxygen- and carbonate carbon-isotope stratigraphy both from bulk and shells (‰ VPDB; from Křížová et al., 2024), organic carbon isotope stratigraphy (‰ VPDB), total organic carbon (TOC, wt. %) and phosphorus concentration (Ptot ppm) from this study. Interval (1–4) chronostratigraphy and OAE-2 interval (grey area) after Křížová et al. (2024). VPDB – Vienna Peedee belemnite.

their shells (RP), capped by 3 m of *Chondrodonta* floatstones (CH). Interval 3 (40–60 m) consists of two floatstone beds with large gastropods (GP) and in an interval dominated by WP facies. Between 50 and 60 m, thick layers of rudist floatstone (RF) are also present.

Interval 4 (60–70 m) is marked by very thick beds of mudstone with micropeloids (MW) and wackestone with microcavities (WV), alternating with thinner beds of PP and RF. Fenestrae, cement-filled vugs, and emersion surfaces are found only in these top 10 m.

4.1.2.1. Organic geochemistry: $\delta^{13}C_{org}$ and TOC. The $\delta^{13}C_{org}$ is scattered, but broadly shows an inverse trend to the $\delta^{13}C_{carb}$ data. Tables with $\delta^{13}C_{carb}$ and $\delta^{18}O$ isotopic data (bulk and shells) from the Devetachi succession are provided in the SI. A total of 36 samples were analyzed to build the $\delta^{13}C_{org}$ profile through the Devetachi section. The values vary between −25.5 ‰ and −21.3 ‰ (Fig. 4) and display a broad positive excursion from 0 to 13 m. Across the entire lithostratigraphic interval 2, the $\delta^{13}C_{org}$ values start to decrease, reaching a minimum of −26.6 ‰ between 26 and 29 m from the base. In the last portion of the isotopic curve (stratigraphic intervals 3 and 4), the $\delta^{13}C_{org}$ rise again in a second, less negative, broad positive excursion, peaking at −21.9 ‰ around meter 53.

The TOC values are relatively low throughout the entire section, ranging from a minimum of 0.03 % to a maximum of 0.18 %, reached at 12 m from the base, corresponding to the first positive excursion of the $\delta^{13}C_{org}$ curve. Due to the very low TOC values, the other parameters obtained from Rock-Eval Pyrolysis analysis (HI, OI, T_{max}) are unreliable and therefore hamper a precise characterization of the organic matter type.

4.1.2.2. Total phosphorus concentration. A total of 42 samples were analyzed for total phosphorus content (P_{tot}). The average P_{tot} is 18 ppm with most values ranging from 5.8 to 42.6 ppm (Fig. 4). Two samples display 301 and 132 ppm, which are values much higher than the P_{tot} average (see supplementary information). These two outliers correspond to the foraminiferal wackestone (WF) and microbioclastic packstone (MP) facies that do not show signs of diagenetic alteration, and are close to laminated bindstone (LB). If the two outliers are excluded, the P_{tot} profile shows a fluctuating trend, with three spikes of relatively positive values (Fig. 4). The first positive P_{tot} spike is found in the lowest 10 m of the section, with a maximum of 29.2 ppm. This is immediately followed by a second rise in P_{tot}, with a second maximum of 31 ppm at 17.2 m. The third and final positive P_{tot} fluctuation is found at 38 m where at the highest peak is 42.9 ppm. From here, the P_{tot} values remain relatively high (another peak of 42.9 ppm at about 53 m) and only decrease towards the top of the section (Fig. 4).

4.1.3. Apennine Carbonate Platform

4.1.3.1. Raia del Pedale. A detailed geochemical, sedimentological, and petrographic study was carried out on the OAE-2 interval of Raia del Pedale (RdP) by Frijia et al. (2019). The section is 70 m thick and characterized by meter-scale subtidal–peritidal cycles containing benthic foraminifera, green algae, molluscs (mainly rudists), ostracods, and microproblematica (*Thaumatoporella* algae), indicating deposition in an inner setting of a carbonate platform. Two distinct intervals of slightly argillaceous “dark” laminites (LAM1 and LAM2 in Fig. 5) have been reported at the onset of the OAE-2 and during the plateau phase of the $\delta^{13}C$ curve (Frijia et al., 2019). The interval corresponding to OAE-2 at RdP and the position of the most relevant facies are presented in Fig. 5.

4.1.3.2. $\delta^{18}O$ shells chemostratigraphy. The 19 bivalve samples analyzed for $\delta^{18}O$ have values ranging from a minimum of −4.5 ‰ to a maximum of −3.4 ‰ (average −3.8 ‰). The $\delta^{18}O$ shell profile shows an overall decreasing trend from the onset of the OAE-2 to its which is, however, interrupted by a prominent interval of relatively positive values (between −3.37 ‰ and −3.29 ‰). This interval corresponds to the trough phase of the C-isotope curve (Fig. 5). After this positive shift the $\delta^{18}O$ profile, shows a pronounced negative inflection correlatable with the peak b of the $\delta^{13}C_{carb}$ excursion. Here the most negative $\delta^{18}O$ values are found (−4.43 ‰). From this point the $\delta^{18}O$ curve returns to more positive values within a general decreasing trend to top of OAE-2.

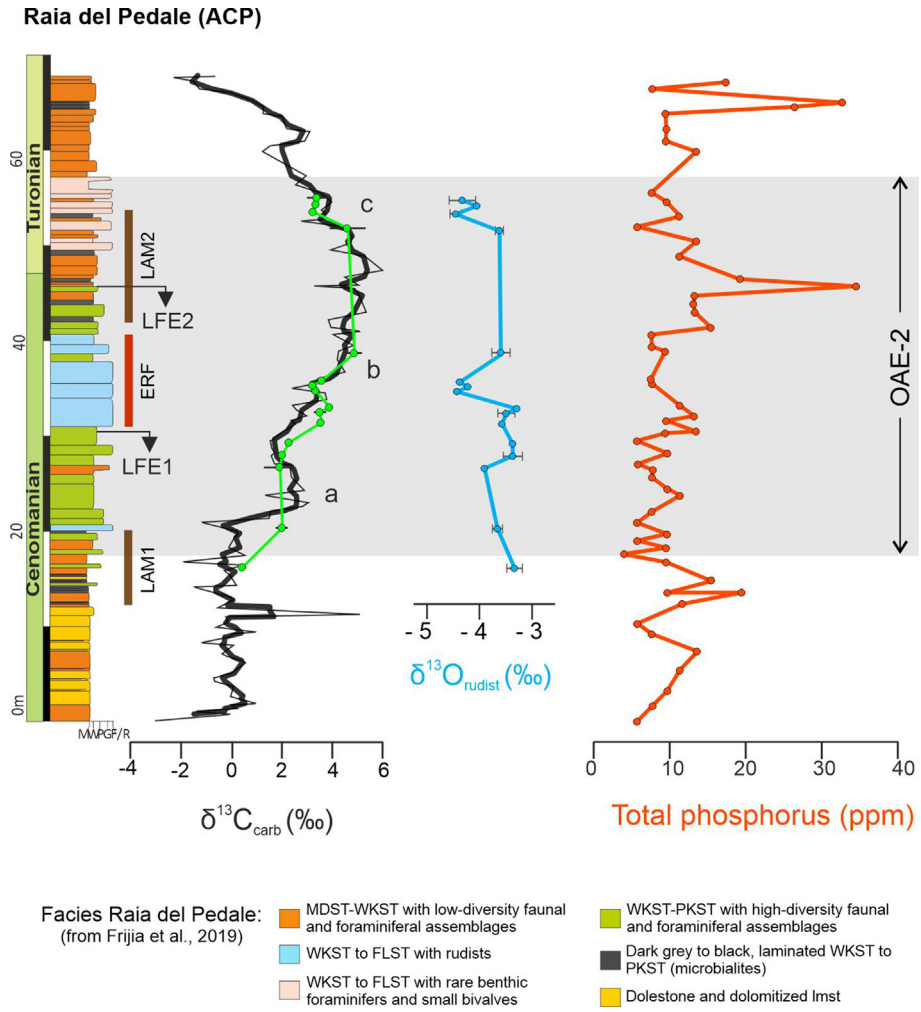

Fig. 5. Raia del Pedale section: lithological log with defined lithofacies, inorganic carbon-isotope stratigraphic profile (‰ VPDB) from bulk samples (thick black line represents the three-point moving average), characteristic $\delta^{13}C$ peaks and trough (peaks a, b, c), and OAE-2 interval (gray area) as defined in from Frijia et al. (2019). $\delta^{18}O$ (‰ VPDB) and Ptot concentration (ppm) profiles were obtained in this study.

4.1.3.3. Raia del Pedale: total phosphorus concentration. At RdP the P_{tot} content ranges from 3.8 to 34.5 ppm (Fig. 5). P_{tot} values exhibit a fluctuating trend divided into three main positive excursions (Fig. 5): (1) The first one (between 13 and 15 m) comprises a maximum value of 19 ppm, corresponding to the lower portion of the first "laminites" defined by Frija et al. (2019; LAM 1 in Fig. 5); (2) the second positive P_{tot} excursion occurs between 41 and 47 m, with the highest value of 34.5 ppm (at 45.7 m). This corresponds to the plateau phase of the $\delta^{13}C$ curve and correlates with the lower part of the second "laminites" of Frijia et al. (2019; LAM 2 in Fig. 5). (3) The third and last positive P_{tot} sharp excursion coincides with a narrow interval between meters 64 and 65, above the OAE-2 interval (Fig. 5).

5. Interpretation and discussion

5.1. Stable isotope signal preservation

The carbon and oxygen isotopic signal in shallow-water carbonates can deviate from the open-ocean global signal due to various processes (e.g. syn- and post-depositional diagenetic alteration, biological fractionation, local paleoceanographic conditions; Marshall, 1992; Immenhauser et al., 2008; Swart and Oehlert, 2018). Recent studies of the CTB interval in shallow-water carbonate sections have proven that reliable high-resolution $\delta^{13}C$ curves can be obtained by microsampling micrite matrix, which occurs either as calcareous mudstone or as a matrix in granular bioclastic facies (Parente et al., 2007; Frijia et al., 2015; Del Viscio et al., 2022; Křížová et al., 2024). Several studies have demonstrated that, although this material can be partly the product of diagenesis (Dickson and Coleman, 1990), under favorable conditions it can preserve the major trends and excursions of the pristine marine signal (Weissert et al., 1985; Joachimski 1994; Immenhauser et al., 2002).

Traditionally, the absence of $\delta^{13}C$ vs. $\delta^{18}O$ covariance is used as an indicator of unaltered isotopic composition (Frijia et al., 2015; Del Viscio et al., 2022 and reference therein), although the presence of covariance is not by itself a definitive indication of diagenesis (Grotzinger et al., 2011). In the Monrupino section, there is no covariance in $\delta^{13}C$ and $\delta^{18}O$ results (Fig. 6A–C), suggesting that neither mixing-zone diagenesis, nor facies type influenced samples preservation (Fig. 6A: $R^2_{MR} = 0.022$). Furthermore, all facies average values plot within the Cretaceous well-preserved "low-latitude" biotic calcite field (Veizer and Prokoph, 2015; green rectangle in Fig. 6C). Lithofacies associated with restricted intertidal and inner platform settings (LB, WV, and DW facies) show more depleted $\delta^{13}C$ and $\delta^{18}O$ values, as also observed in the Devetachi section (Křížová et al., 2024) (Fig. 6C). Rudist and *Chondrodonta* shells with well-

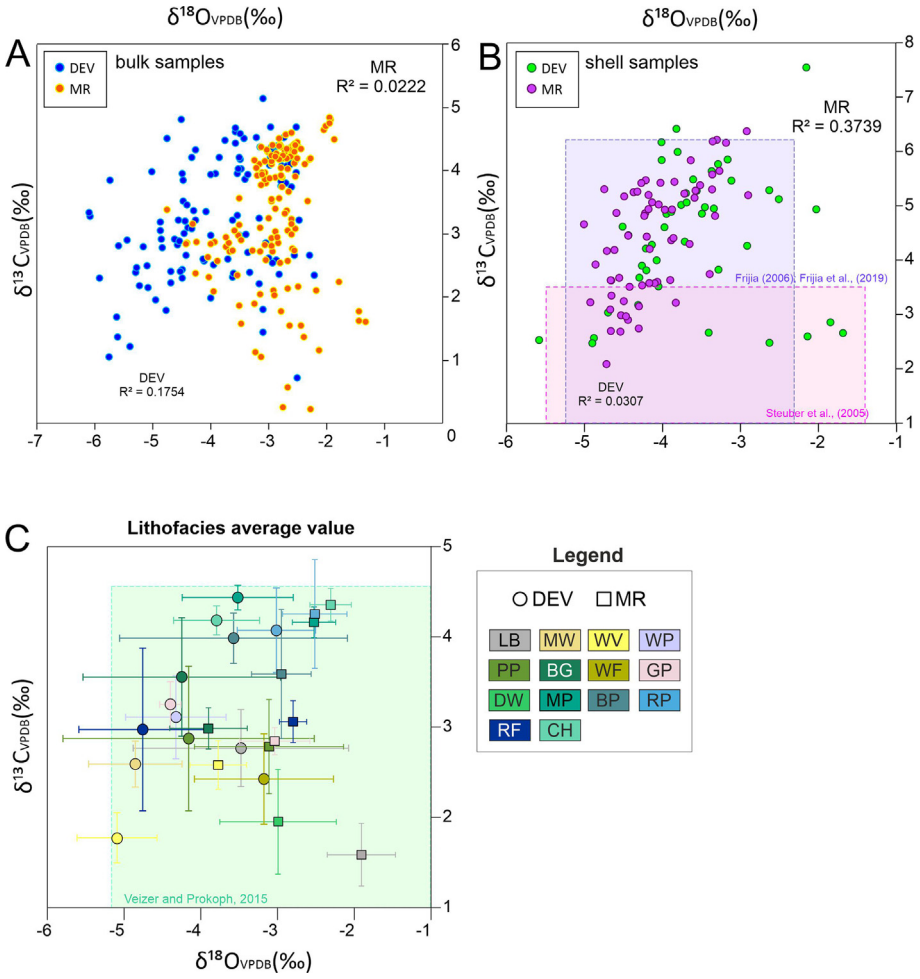

Fig. 6. Cross-plot of carbonate $\delta^{18}O$ vs. $\delta^{13}C$ values for the Monrupino (MR - this study) and Devetachi (DEV from Křížová et al., 2024, for comparison) sections. (A) Individual bulk samples $\delta^{18}O$ vs. $\delta^{13}C$ for DEV (blue dots) and MR (orange dots); (B) Individual rudist samples $\delta^{18}O$ vs. $\delta^{13}C$ for DEV (green dots) and MR (purple dots). The bulk dataset shows no covariance between O and C isotopic values. The shell dataset for MR shows a slightly positive covariance but the shell data are consistent with findings of (Frijia et al., 2015, 2019). (C) Average $\delta^{18}O$ and $\delta^{13}C$ of individual lithofacies for MR (squares) and DEV (circles, for comparison), and error bars indicate the standard deviation of the averages. All lithofacies fall inside the area (light green rectangle) which represents the well-preserved biotic calcite of Phanerozoic shallow marine tropical-subtropical carbonate (Veizer and Prokoph, 2015).

preserved original microstructure from Monrupino exhibit a slight covariance of $\delta^{13}C$ and $\delta^{18}O$ composition (Fig. 6B: $R^2_{MR} = 0.37$). Nonetheless, most rudist shells isotopic values from the Monrupino section align with findings from Frijia et al. (2015, 2019), derived from the late Cenomanian–Campanian rudist shells from the ACP (blue rectangle in Fig. 6B). They also match the $\delta^{18}O$ composition of well-preserved Late Cretaceous rudists studied by Steuber et al. (2005) (pink rectangle in Fig. 6B) and are in line with the values measured in rudist shell fragments from the nearby Devetachi section (Křížová et al., 2024). This evidence points to good preservation of $\delta^{13}C$ and $\delta^{18}O$ composition of the shells in the Monrupino section.

5.2. Regional to supra-regional OAE-2 correlations of western Tethys carbonate platforms

The Devetachi and Monrupino sections show similar $\delta^{13}C$ carbon fluctuations both in the bulk and bivalve shell curves for the upper Cenomanian–lower Turonian interval.

This allows for high-resolution correlations between the two sites. The main isotopic signature used for correlation is the large positive $\delta^{13}C$ shift (up to ~5 ‰) observed for the bulk and shell curves in both areas. Whilst slightly more positive and more variable values are noted for the shell curve compared to the bulk, the correlation potential is still high. In particular, in the Devetachi section, the positive excursion can be correlated with the OAE-2 CIE documented by Křížová et al. (2024). The high-resolution $\delta^{13}C$ curves of Devetachi and Monrupino, and in particular the shells profiles, capture the complex structure of the $\delta^{13}C$ excursion at the Cenomanian/Turonian boundary shown by the European reference section at Eastbourne, England (Paul et al., 1999; Jarvis et al., 2006, 2011; Falzoni and Petrizzo, 2020, Fig. 7).

Integrating bulk rock and shell $\delta^{13}C$ profiles in both studied sections, we identified the four main segments of the OAE-2 described in the reference section (Paul et al., 1999) and the three positive peaks a, b and c introduced by Jarvis et al. (2006). Some of these isotopic features were identified with a high degree of confidence in the Devetachi section, thanks to the close match between the bulk and shells curves in this area, with the Eastbourne reference profile. In the Monrupino section the absence of a clear trough in both the bulk and shell $\delta^{13}C$ records, makes more uncertain the identification of isotopic peaks a and b. Nevertheless, the good match between isotopic correlations and facies occurrence in both

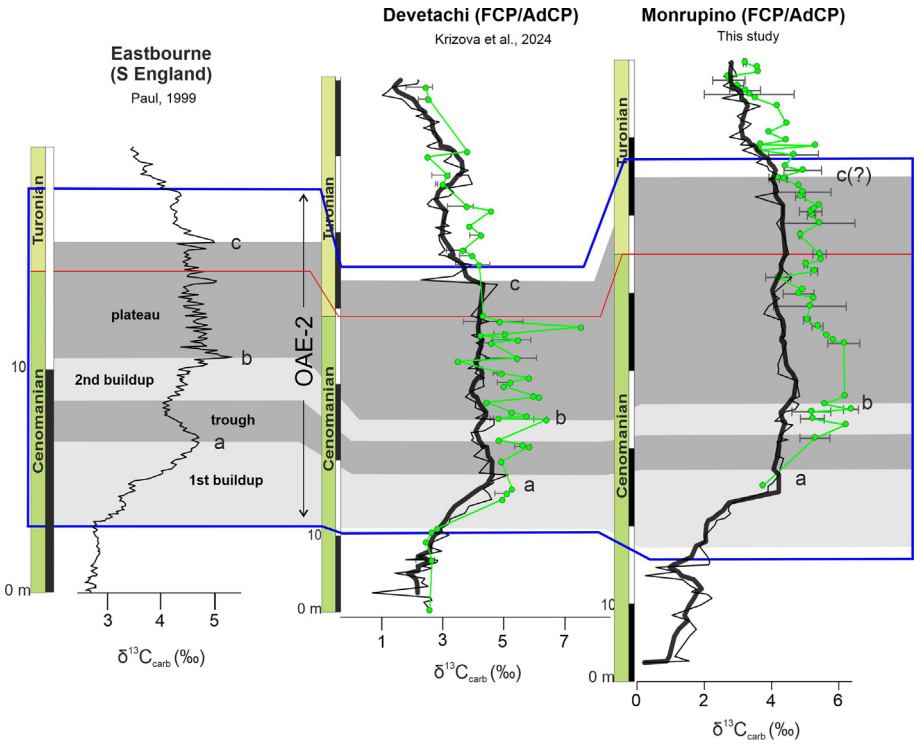

Fig. 7. Chemostratigraphic correlation of the Monrupino and Devetachi sections bulk-rock $\delta^{13}C$ profiles with the OAE-2 standard reference section of the Eastbourne Chalk (Sussex, England; Paul et al., 1999). Thick black lines are 5 points moving averages. The interval representing the OAE-2 (blue lines and gray areas) are placed after chemostratigraphic correlations using characteristic $\delta^{13}C$ segments (peaks and troughs as defined in Paul et al., 1999) and the positive a, b, and c pecks introduced by Jarvis et al. (2006). The Plenus Cold Event (PCE - light blue vertical bars) interval after Jenkyns et al. (2017). The continuous red line indicates the Cenomanian/Turonian boundary (CTB).

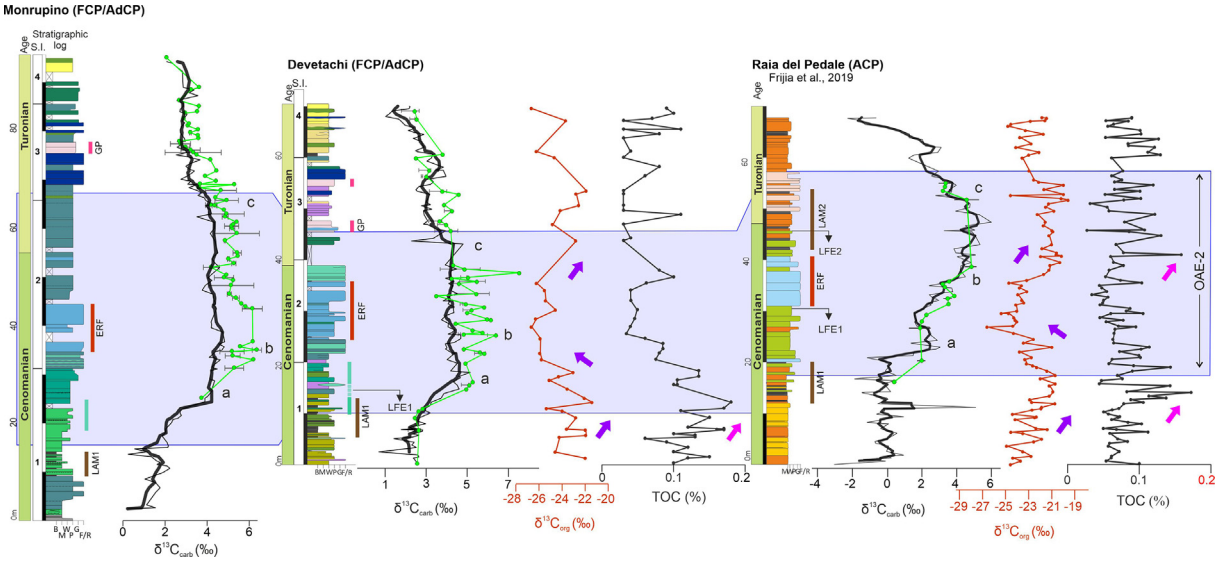

Fig. 8. Geochemical (δ^{13}Ccarb, δ^{13}Corg, TOC) and lithological correlation of Tethyan shallow-water carbonate sections from the FCP (δ^{13}Ccarb from bulk – black curve, and bivalve shells – green curves) and ACP (Raia del Pedale section, South Italy; Frijia et al., 2019; black line: bulk-rock data, green line: bivalve shells $\delta^{13}C$ data). Devetachi δ^{13}Ccarb and lithological data are from Křížová et al. (2024) whereas δ^{13}Corg and TOC data for DEV section are from this study. Monrupino geochemical and lithological data are from this study; Vertical red bars ERF indicate the interval rich in elongated rudist fragments. Vertical pink bars GP indicate the interval with large gastropods. Vertical green bars next to the Monrupino and Devetachi sedimentological logs indicate the presence of calcispheres. The vertical brown bars (LAM1 and LAM2) indicate dark laminite intervals as defined by Frijia et al. (2019). The LFE 1–2 indicate the two levels of larger benthic foraminifera extinction after Parente et al. (2008). The OAE-2 interval is represented by a light blue area.

sections suggest that the position of the OAE-2 segments at Monrupino is quite robust (Fig. 7).

The good correlation between the presented shallow–waters sections and the reference pelagic $\delta^{13}C$ curves further reinforces the conclusion that diagenesis, heavily affecting shallow water environments, has not obscured the original marine isotopic signal of the FCP successions.

The $\delta^{13}C$ correlation allows the evaluation of facies evolution in the FCP in the context of the OAE-2. As shown in Fig. 8, centimeter-thick laminated bindstones (LB facies; brown vertical

bar - LAM1), and levels with sporadic calcispheres (green vertical bar) are present in both successions. LAM1 preceedes and follows the onset of the OAE-2, suggesting a deterioration of the environmental conditions pre-OAE-2. The calcispheres interval coincides with the onset of the excursion. These are more abundant in the Monrupino section, associated with the "Zolla member", and indicate a slight relative sea level rise, already demonstrated in many sections pre OAE-2 in the FCP (e.g. Drzewiecki and Simo, 1997; Brčić et al., 2017). Abundant *Chondrodonta* floatstone beds and approximately 10 m of thin-elongated rudists fragments packstone/floatstone are the dominating facies through the trough phase of the carbon-isotope curve. The presence of distinctive gastropod facies (pink vertical bar – GP, Fig. 8) is a shared lithostratigraphic marker between the two FCP sections, occurring at the end of the $\delta^{13}C$ plateau phase. Lastly, facies suggesting very shallow depositional conditions with ephemeral emersions (WV facies) are abundant in both sections following the end of the OAE-2.

Chemostratigraphic correlation of the FCP $\delta^{13}C$ records with that from the ACP (Raia del Pedale section) allows the identification of close similarity in facies and geochemistry evolution (Fig. 8). In both areas, peritidal to shallow lagoonal facies dominate throughout the entire OAE-2 interval. In both carbonate platforms pre-OAE-2, OM-rich laminated facies (LAM1, Fig. 8) occur, followed by a thick interval of massive/crudely bedded floatstone-rudstones with thin elongated rudist fragments (ERF - red vertical bar, Fig. 8) between the isotopic peaks b and c of the $\delta^{13}C$ curve. Above this interval, both areas experienced a decrease in faunal diversity of benthic foraminifera and rudists until the end of OAE-2. Interestingly, the thickness of the OAE-2 interval (40–50 m) is comparable between the studied FCP and ACP sections and the $\delta^{13}C$ bulk and shells curves from the ACP present overlapping values. In contrast, the FCP $\delta^{13}C$ profiles show a clear offset between the shell and the bulk curves (Fig. 8). Furthermore, in the FCP sections the shells yield higher $\delta^{13}C$ values than in the ACP. The reason behind these patterns is not clear but might be linked to larger internal variability of shell isotopic values in the FCP samples than in the ACP and/or to local variations of the $\delta^{13}C$ pool. The shells curves in all sections preserve in detail the OAE-2 $\delta^{13}C$ record and prove to be a very robust tool for $\delta^{13}C$ correlation. This finding is very relevant for successions where bulk data are not reliable (e.g. diagenetically altered).

The Devetachi and Raia del Pedale sections also share comparable TOC content (Fig. 8), with average values of 0.08 % for Raia del Pedale and 0.09 % for the Devetachi section. These values are typical of carbonate platforms (Hunt, 1995). The highest TOC values are observed in both sections within the laminites-dominated interval (LAM1) predating the onset of OAE-2 (pink arrows in Fig. 8). A second, minor increase in TOC is also observed at Raia del Pedale corresponding to the second laminites interval (Frijia et al., 2019, LAM 2 of Fig. 8). In the Devetachi section, the upper portion of the OAE-2 interval, only comprises one thin bed of dark laminites, most likely due to the presence of frequent gaps (lack of exposed outcrop) in this part of the section. This may be also true for the Monrupino section, where no OM-rich laminites were found, potentially for the same reason (Fig. 8).

The $\delta^{13}C_{org}$ curves from the Devetachi and Raia del Pedale sections show two distinct broad peaks separated by a trough interval with the lowest $\delta^{13}C_{org}$ values occurring in both sections between peaks a and b of $\delta^{13}C_{carb}$. The first positive broad peak aligns with the onset of OAE-2, as defined by the $\delta^{13}C_{carb}$ profile, whilst the second occurs after the b peak (Fig. 8).

In both the Devetachi and Raia del Pedale sections (Fig. 8), the $\delta^{13}C_{org}$ curve shows these positive shifts corresponding to the "laminites" units of Frijia et al. (2019, LAM 1 and LAM2 of Fig. 8). According to Frijia et al. (2019), the $\delta^{13}C_{org}$ fluctuations at Raia del Pedale do not relate to changes in OM type (continental vs. marine), but rather reflect a shift in productivity, driven by photosynthetic microorganisms/bacterial activity, resulting in an in-situ fractionation of carbon isotopes. The close correspondence between laminites intervals, $\delta^{13}C_{org}$ and a TOC shift between the RdP and DEV suggest a common mechanism and a likely coeval increase of microbial productivity associated to the OAE-2 perturbations.

5.3. Paleotemperature reconstruction

The Cenomanian was characterized by rising sea-surface temperatures that reached maximum values during the early Turonian both in open seas and marginal/coastal areas (e.g., O'Brien et al., 2017; Huber et al., 2018; Křížová et al., 2024). The trend was interrupted only by a transient cooling episode (~150 kyr long) in the latest Cenomanian, which Gale and Christensen (1996) named "Plenus Cold Event" (PCE). Oxygen isotopes measured on bulk carbonates and macrofossil shells (e.g., Paul et al., 1999; Tsikos et al., 2004; Voigt et al., 2006; Jarvis et al., 2011; O'Brien et al., 2017; Falzoni and Petrizzo 2020) have been used extensively as paleotemperature proxies in several basins in Northern Europe, the Western Interior Seaway (WIS), and the North-Equatorial Atlantic Ocean, to better identify these important paleotemperature variations during the OAE-2 and comparing those with faunal changes (faunal turnovers, originations, extinctions). Recently, high-resolution paleotemperature reconstructions in upper Cenomanian – middle Turonian shallow-water carbonates have been provided by Křížová et al. (2024), based on the $\delta^{18}O$ analysis of rudist shells from the Devetachi section. The Křížová et al. (2024) data are here integrated with $\delta^{18}O$ analyses from Monrupino and Raia del Pedale sections to constrain, for the first time, the temperature evolution in different Tethyan carbonate platforms during OAE-2 and to compare it with the deep-water records.

Considering the highly debated issue of deriving absolute temperature from mollusc $\delta^{18}O$ data in coastal areas (Křížová et al., 2024), here we interpret oxygen isotope data in terms of cooling or warming trends (Fig. 9), rather than absolute temperatures.

The Devetachi, Monrupino and Raia del Pedale $\delta^{18}O$ profiles show a generally similar trend, with decreasing $\delta^{18}O$ (suggesting warming) spanning the entire OAE-2, interrupted by a positive inflection (suggesting cooling), occurring between peaks a and b of the $\delta^{13}C$ excursion. This cold snap correlates with the interval of cooling identified by geochemical TEX_{86} (Forster et al., 2007, Fig. 9), and $\delta^{18}O$ proxies (e.g. Falzoni and Petrizzo, 2020) from pelagic settings and corresponding to the PCE. According to our chemostratigraphic correlations, we can place the PCE in the studied sections, between the peak a and b of the $\delta^{13}C$ curve, where the $\delta^{18}O$ shell profile presents an interval of more positive values (Fig. 9).

In some instances, local factors might have a substantial impact, creating a local response to global CO_2 fluctuations (O'Brien et al., 2017 and references therein), which may generate different reconstructed temperature fluctuations at different sites (O'Connor et al., 2020). This is not the case for the studied sections, which record coeval $\delta^{18}O$ fluctuations to that observed in deep-water sites, potentially implying that cooling and re-oxygenation of bottom waters occurred nearly simultaneously in the neritic and pelagic settings. The PCE thermal instability may have triggered increased mixing of water masses with the replenishment of surface productivity via upwelling (Forster et al., 2007) and was likely sustained by the coeval introduction of a range of redox-sensitive trace metals into global ocean waters (Jenkyns et al., 2017; Clarkson et al., 2018; Sweere et al., 2018). According to Parente et al. (2008) and Frijia et al. (2019), the upwelling of deep, nutrient-rich

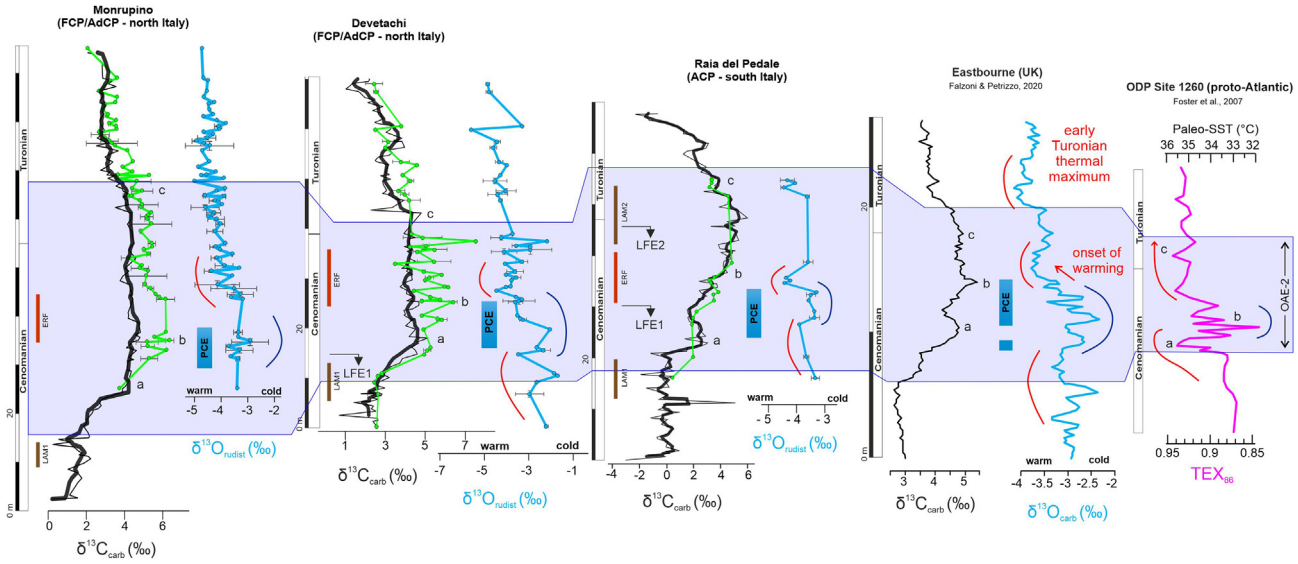

Fig. 9. Correlation between the Devetachi, Monrupino and Raia del Pedale sections $\delta^{18}O$ curves obtained from well-preserved bivalve shells and the reference pelagic sections from Eastbourne (UK; Paul et al., 1999) and TEX^{86} profile from ODP Site 1260 (proto- Atlantic; Forster et al., 2007). The green curve superimposed on the black $\delta^{13}C$carb curve corresponds to the inorganic carbon isotope ratio obtained from well-preserved bivalve shells (mainly rudists) in the studied shallow-water sections (geochemical data from Křížová et al., 2024; Frijia et al., 2019, this study). The Plenus Cold Event (PCE) (vertical blue bars) interval is placed after Jenkyns et al. (2017). Warming (red) and cooling (blue) shifts in $\delta^{18}O$ curves are taken from Falzoni and Petrizzo (2020) and applied to the studied sections. ERF indicates the elongated rudist fragments rich interval. The vertical brown bars (LAM1 and LAM2) indicate dark laminite intervals as defined in Frijia et al. (2019). The LFE 1–2 indicates the two levels of larger benthic foraminifera extinction after Parente et al. (2008). The OAE-2 interval is represented by the light blue area.

waters flooded over neritic settings and transported excess nutrients on isolated shallow-water platforms triggering a cascade of biological changes including the extinction of larger foraminifera. We explore this possibility in the following section, discussing the P changes across the OAE-2 in the FCP and ACP.

5.4. Phosphorus

The key factors triggering deposition of black shales in different Tethyan locations during the OAE-2 were likely the combination of enhanced primary productivity and increased preservation of organic matter (OM), due to dysoxic to anoxic bottom-water conditions (Huber et al., 2002; Kuypers et al., 2002; Erba et al., 2004; Hardas and Mutterlose, 2007; Mort et al., 2007; Friedrich et al., 2008). The source of nutrients required to fuel high marine primary productivity during the OAE-2 remains uncertain. Various proposed mechanisms include strong up-welling of nutrient-rich intermediate and deep waters (Parrish and Curtis 1982; Einsele and Wiedmann 1983; Arthur et al., 1987; Poulsen et al., 2001), increased hydrothermal input of biolimiting nutrients and trace metals (Sinton and Duncan 1997; Kerr 1998; Larson and Erba 1999; Turgeon and Creaser 2008), leaching of nutrients from flooded continental shelf areas (Jenkyns 1980; Erbacher et al., 1996; Hilbrecht et al., 1996; Jarvis et al., 2002), and increased riverine nutrient delivery in a warm climate setting, generally characterized by intensified hydrological cycle and weathering (Manabe and Bryan Jr, 1985; Handoh and Lenton 2003; Bjerrum et al., 2006; Wagner et al., 2007).

To sustain increased marine productivity and ocean anoxia, enhanced P regeneration in response to bottom-water oxygen depletion was crucial, provided that nutrient P was upwelled into the photic zone (Van Cappellen and Ingall, 1994). Modeling studies indicate that prevailing anoxic conditions during black shale deposition in the OAE-2 led to increased P release from organic matter (Bjerrum et al., 2006; Tsandev and Slomp 2009; Clarkson et al., 2018). In the studied section, however, conditions remained mostly oxic throughout the whole of OAE-2 and therefore P accumulation appears to be more complex and possible the results of several interplaying mechanisms. Furthermore,

P distribution in sedimentary successions can be affected by changes in lithology/facies and sedimentation rates. In order to overcome this possible biases, we also calculated P mass accumulation rates to account for variable sedimentation rates and lithological changes in P content (Bomou et al., 2013 and reference therein).

The patterns of P_{tot} curves at Raia del Pedale and Devetachi sections are comparable and exhibit similar variations and absolute values (Fig. 10). In the studied Tethyan sections P_{tot} values remain consistently low throughout the entire OAE-2 interval (Raia del Pedale ranging from 4 to 35 ppm and Devetachi between 6 and 43 ppm) except for two stratigraphic intervals. P_{totmar} curves show a marked correspondence with P_{tot} profiles (Fig. 10), highlighting two prominent peaks/intervals of P enrichment. The similarity between P_{tot} and P_{totmar} curves suggests that the observed P fluctuations can be considered primary and not biased by differences in sedimentation rate and/or facies. A first interval of high P content occurs in both sections straddling the onset of OAE-2 (first lower blue arrow, Fig. 10). Several studies have observed an increase in total sedimentary phosphorus predating OAE-2 and the associated significant rise in primary productivity (Mort et al., 2007, 2008; Tsandev and Slomp, 2009; Kraal et al., 2010).

The increase of P delivery would have been driven by enhanced continental weathering and sustained by the transition from oxic to anoxic conditions resulting in decreased phosphorus burial efficiency. Increasing seawater P concentrations may have promoted an expansion of anoxia (AE1 of Clarkson et al., 2018). This, in turn allowed better preservation of OM, and pore waters switched from being a P sink to a P source sustaining the productivity-driven $\delta^{13}C$ positive excursion in a positive feedback loop (Mort et al., 2007).

Such a scenario is not supported by the results from the investigated sections. Indeed, the presence of facies relatively enriched in TOC (laminites) are found both in the FCP and ACP pre-OAE-2, but these are alternated with organic-lean beds. Furthermore, there is no paleontological or clear geochemical evidence

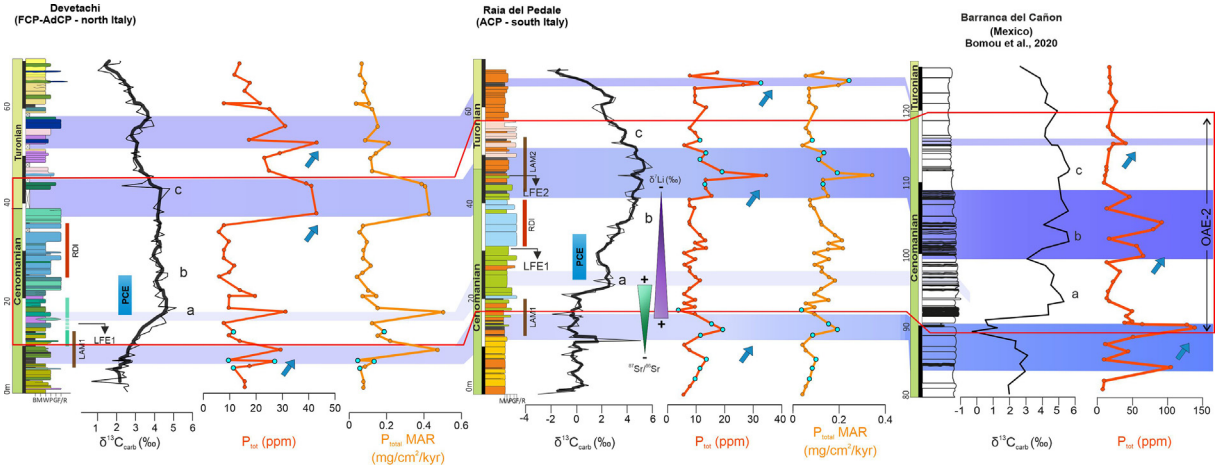

Fig. 10. Correlation of phosphorus Ptot and Pmar (shaded purple panels) maxima concentrations from Devetachi and Raia del Pedale sections with the coeval shallow-water section of Barranca del Cañon (Mexico; Bomou et al., 2020). The $\delta^{13}C$ curve of Raia del Pedale is from Frijia et al. (2019) and the $\delta^{13}C$ curve of Devetachi is from Křížová et al. (2024). Purple correlation areas are associated with the positive fluctuations in Ptot and their colour intensity varies according to the absolute value of concentration (ppm) (e.g., absolute values at Raia del Pedale and Devetachi are lower than those observed at Barranca del Cañon). Plenus Cold Event (PCE) (vertical blue bars) interval after Jenkyns et al. (2017). The shaded triangles indicate the increasing (+) or decreasing trends (−) of two isotope proxies used to infer weathering intensity. The radiogenic $^{87}Sr/^{86}Sr$ pulse (green triangle from Frijia and Parente (2008) and the $\delta^{7}Li$ isotopes decreasing trend (purple triangle from Pogge von Strandmann et al., 2013) suggest increased weathering rates just before the onset of OAE-2. Vertical green bars beside Monrupino and Devetachi lithologs indicate the presence of calcispheres. The vertical brown bars (LAM1 and LAM2) indicate dark laminite intervals as defined in Frijia et al. (2019). LFE 1−2 indicates the two levels of larger benthic foraminifera extinction after Parente et al. (2008). The OAE-2 interval is represented by the red lines and the peaks a, b, and c are placed after Fig. 7.

suggesting anoxic conditions (this study; Zhou et al., 2015; Frijia et al., 2019). Therefore, the possibility of phosphorus recycling due to the occurrence of anoxic−dysoxic conditions in the studied shallow−water settings seems unlikely. This suggests that the P accumulation in the Devetachi and Raia del Pedale sections was rather the result of the combined P delivery from external sources and/or increased P concentration associated with biological activity.

In both the Devetachi and Raia del Pedale sections, the high P_{tot} accumulation pre-OAE-2 is found in the "laminites" interval (LAM1, Fig. 10), thus suggesting peculiar phosphatic accumulations linked to benthic activity of microbial mats (Krajewski, 2011). Cyanobacteria directly absorb phosphorus from the surrounding environment, sourced from adjacent sediments, waters, or other biological processes promoting phosphorus accumulation or fixation (Bhardwaj et al., 2024). In many microbialites, mineralization processes promoted by bacteria and cyanobacteria, convert organic compounds containing phosphorus into more stable inorganic compounds. The higher phosphorus concentrations in the laminite levels at Raia del Pedale and Devetachi sections, although linked to preferential enrichment in P by microbial activity, would have required substantial levels of P in the surrounding waters. Enhanced P influxes, pre-OAE-2, might have been linked to increase in continental weathering as suggested by Sr and Li isotope shifts recorded at the onset of the OAE-2 (Frijia and Parente, 2008; Pogge von Strandmann et al., 2013; see Fig. 10). Evidence of total P fluctuations related to changes in detrital input are observed in coeval sections in Tibet (Bomou et al., 2013) and Mexico (Bomou et al., 2020). Figure 10 shows the good correlation between the P_{tot} abundance records in the Devetachi and Raia del Pedale sections and those from the Barranca del Cañon section, in the Guerrero-Morelos Platform of Mexico (Bomou et al., 2020). Interestingly the highest P_{tot} concentrations in the Mexican section are also found in stratigraphic intervals rich in laminites (darker beds in Fig. 10). This points to a link between these facies, the P enrichment, and continental weathering, which may have caused episodic mesotrophy and fluctuating redox conditions in a usually oligotrophic and oxic depositional environment. P_{tot} values decrease immediately after peak a of the $\delta^{13}C$ curves and stay low across the PCE in both studied sections and in the Mexican platform.

A second interval characterized by high P_{tot} concentrations in both the Devetachi and Raia del Pedale sections starts after peak b of the $\delta^{13}C$ curve (the so-called plateau phase of the OAE-2, Fig. 10). This is associated with the second "laminites" interval (LAM2 in Fig. 10) of Frijia et al. (2019), again suggesting a possible link between these facies and the P_{tot} fluctuations. In the carbonate platform of Mexico, a second peak of P_{tot} values is also noted in a correlatable, but not microbially laminated interval.

A second injection, post PCE, of CO_2 by volcanic activity has been proposed based on trace element enrichment and Os isotopes data (Snow et al., 2005; Eldrett et al., 2014; Du Vivier et al., 2015), whereas $\delta^{18}O$ and U isotopes data suggest a second increase of temperatures (after the drop at the PCE) and the return of widespread anoxia (e.g. Clarkson et al., 2018; Falzoni and Petrizzo, 2020). Geochemical evidences, based on trace element enrichment data (Snow et al., 2005; Eldrett et al., 2014) and Nd isotopes from Eastbourne (Zheng et al., 2013), also suggest a second pulse of enhanced global weathering influx. Nonetheless, this interpretation is debatable. The second interval of high P_{tot} values in the studied sections could have, slightly, different explanations than the one occurring pre-OAE-2. Parente et al. (2008) argued that during the initial phase of the OAE-2, high productivity and excess organic carbon burial were mainly localized at the margins of the Atlantic Ocean. The thermal instability during the PCE caused the collapse of thermal stratification of ocean water triggering the delivery of high amounts of nutrients to surface waters. These large influxes of nutrients might have affected also neritic settings and the isolated tropical carbonate platforms of the Tethyan realm. As a result, the positive fluctuations in total phosphorus concentration we observed during the plateau phase of the OAE-2 $\delta^{13}C$ curve, could be attributed to an increase in nutrient availability, caused by changes in ocean circulation and upwelling, with a (minor) contribution from terrestrial weathering. Interestingly, this second pulse in P_{tot} concentrations and resumed increase in temperatures coincide, in the studied sections, not only with a second interval of abundant deposition of organic-rich laminites, but also with the

final step of extinction of larger benthic foraminifera (LFE 2 in Fig. 10) and a significant rudists extinction event (Philip and Airaud Crumiere, 1991; Steuber et al., 2023; Petrizzo et al., 2025). Křížová et al. (2024) suggested that the observed rate of temperature changes and their magnitude were able to wipe away most of the biotic communities of the carbonate platform at the OAE-2. Nonetheless, the data presented here suggest that a very "unfortunate" series of killing factors rather than temperature alone co-occurred during the OAE-2. These overcame critical thresholds for most carbonate bioproducers (Parente et al., 2008; Frijia et al., 2019; Křížová et al., 2024; Petrizzo et al., 2025), which, therefore, ceased to exist. Only the less specialized groups among benthic foraminifera and the bacteria were able to thrive in these detrimental environmental conditions.

Lastly, it is important to point out that the strong similarities between facies and P_{tot} fluctuations between the western Tethys platforms and the Atlantic ones (Mexico platform) indicate that the evolution of carbonate platforms during the OAE-2 was mainly modulated by global processes. This testifies the high sensitivity of coastal and shallow settings to paleoenvironmental changes associated with OAE-2.

6. Conclusions

A comprehensive study including geochemical (P_{tot}, $\delta^{13}C_{carb}$, $\delta^{13}C_{org}$, TOC, $\delta^{18}O$), sedimentological, and stratigraphic analyses was carried out on three successions spanning the CTB in the Friuli Carbonate Platform of northern Italy and the Apennine Carbonate Platform (ACP) in southern Italy. Fifteen lithofacies and four lithofacies associations were identified in the FCP, indicating deposition in an inner platform setting with intertidal to shallow subtidal facies. For the first time, the interval corresponding to the OAE-2 of the FCP is described in detail, allowing a correlation with the coeval well-studied shallow-water carbonates of the ACP. The comparison reveals similar facies evolution, geochemical and biotic changes during OAE-2. This suggests a similar response of shallow-water carbonate ecosystems to the perturbations associated with the OAE-2. $\delta^{18}O$ analysis on well-preserved bivalve (mainly rudists) shells allowed the reconstruction of paleotemperature trends during the OAE-2 at the studied sites. Oxygen isotopic values are consistent with global warming pulses during the OAE-2, interrupted by a cold interval correlated with the so-called "Plenus Cold Event".

Phosphorus concentrations in the studied sections are in line with the few published global P accumulation curves during the OAE-2, and with the only available record from shallow–water carbonates of Mexico. This suggests a global influence on P accumulation in platform carbonates. Our findings also show that P accumulation in carbonate platforms seems to be associated with different mechanisms: increase in detrital input at the onset of OAE-2, and mainly refueling of surface primary productivity through upwelling, in the late phase of the event. Our results also suggest the important role of bacteria on P accumulation/preservation through various metabolic processes.

The results of this work highlight the multiple possibilities of phosphorus recycling in shallow environments and the multifaceted nature of phosphorus dynamics during OAE-2. Laminites/microbialites-rich intervals are present in both FCP and ACP at specific stratigraphic levels and their abundance is associated with episodes of increased temperature and P (nutrients levels). Conversely, the main bioproducers of late Cenomanian carbonate platforms (benthic foraminifera and rudists) were severely impacted by the increase in temperatures and trophic levels, experiencing a major turnover and extinction before the end of OAE-2. The similarities between the "new world" and "old world" carbonate platform records in terms of geochemical and facies changes, clearly indicate a global control on platform evolution during OAE-2.

CRediT authorship contribution statement

Sahara Cardelli: Writing – original draft, Methodology, Formal analysis, Data curation, Conceptualization. **Barbora Křížová:** Writing – original draft, Investigation, Formal analysis, Data curation. **Michele Morsilli:** Writing – original draft, Investigation, Data curation. **Renato Posenato:** Writing – original draft, Investigation, Data curation. **Thierry Adatte:** Writing – review & editing, Investigation, Formal analysis. **Brahimsamba Bomou:** Writing – review & editing, Formal analysis, Data curation. **Jorge E. Spangenberg:** Writing – review & editing, Formal analysis. **Lorenzo Consorti:** Writing – original draft, Investigation, Formal analysis, Data curation. **Amerigo Corradetti:** Writing – review & editing, Formal analysis. **Marco Franceschi:** Writing – original draft, Investigation, Formal analysis. **Valentina Brombin:** Writing – review & editing, Formal analysis, Data curation. **Gianluca Frijia:** Writing – original draft, Validation, Supervision, Resources, Project administration, Formal analysis, Data curation, Conceptualization.

Declaration of competing interest

The authors declare the following financial interests/personal relationships which may be considered as potential competing interests: Sahara Cardelli reports financial support was provided by International Association of Sedimentologists. If there are other authors, they declare that they have no known competing financial interests or personal relationships that could have appeared to influence the work reported in this paper.

Acknowledgments

Support for this work was provided by a UNIFE research grant FIR 2019 to GF and by a post graduated IAS grant 2021 to SC. We are grateful to Giorgio Tunis for his help in the field and for introducing us to the complex geology of the Friuli Carbonate Platform. We warmly thank Laura Galluccio (Badley Ashton) for proofreading the final version of the manuscript. Finally, the manuscript benefited greatly from the criticism and suggestions of reviewers Ian Jarvis and Mariano Parente and the careful and patient editorial work of Maria Rose Petrizzo.

Data availability

Data will be made available on request.

References

Arthur, M., Schlanger, S.t., Jenkyns, H., 1987. The Cenomanian/Turonian Oceanic Anoxic Event, II. Palaeoceanographic controls on organic-matter producti and preservation. Geological Society, London, Special Publications 26 (1), 401–420.

Bhardwaj, A., Singh, P., Gupta, N., Bhattacharjee, S., Srivastava, A., Parida, A., Mishra, A.K., 2024. Cyanobacteria: a key player in nutrient cycling. In: Cyanobacteria. Elsevier, pp. 579–596.

Bjerrum, C.J., Bendtsen, J., Legarth, J.J.F., 2006. Modeling organic carbon burial during sea level rise with reference to the Cretaceous. Geochemistry, Geophysics, Geosystems 7, Q05008. https://doi.org/10.1029/2005GC001032.

Bomou, B., Adatte, T., Tantawy, A.A., Mort, H., Fleitmann, D., Huang, Y., Föllmi, K.B., 2013. The expression of the Cenomanian–Turonian oceanic anoxic event in Tibet. Palaeogeography, Palaeoclimatology, Palaeoecology 369, 466–481. https://doi.org/10.1016/j.palaeo.2012.11.011.

Bomou, B., Adatte, T., Arnaud-Vanneau, A., 2020. In: Adatte, Thierry, Bond, David P.G., Keller, Gerta (Eds.), Guerrero-Morelos carbonate platform response to the Caribbean-Colombian Cretaceous large igneous province during Cenomanian–Turonian oceanic anoxic event 2. The Geological Society of

American book:" Mass Extinctions, Volcanism, and Impacts: New Developments, vol. 544. GSA. https://doi.org/10.1130/SPE544.
Brčić, V., Glumac, B., Fuček, L., Grizelj, A., Horvat, M., Posilović, H., Mišur, 2017. The Cenomanian–Turonian boundary in the northwestern part of the Adriatic Carbonate Platform (Ćićarija Mtn., Istria, Croatia): characteristics and implications. Facies 63, 1–20.
Brčić, V., Glumac, B., Brlek, M., Fuček, L., Šparica Miko, M., 2021. Cenomanian–Turonian oceanic anoxic event (OAE2) imprint on the northwestern part of the Adriatic Carbonate Platform and a coeval intra-platform basin (Istria and Premuda Island, Croatia). Cretaceous Research 125. https://doi.org/10.1016/j.cretres.2021.104847.
Chiocchini, M., Pampaloni, M.L., Pichezzi, R.M., 2012. Microfacies and microfossils of the Mesozoic carbonate successions of Latium and Abruzzi (Central Italy). Memorie per Servire alla Descrizione della Carta Geologica D'Italia, ISPRA, Dipartimento Difesa del Suolo 17, 269.
Clarkson, M.O., Stirling, C.H., Jenkyns, H.C., Dickson, A.J., Porcelli, D., Moy, C.M., Pogge Von Strandmann, P.A.E., Cooke, I.R., Lenton, T.M., 2018. Uranium isotope evidence for two episodes of deoxygenation during Oceanic Anoxic Event 2. Proceedings of the National Academy of Sciences 115 (12), 2918–2923. https://doi.org/10.1073/pnas.1715278115.
Consorti, L., Arbulla, D., Bonini, L., Fabbi, S., Fanti, F., Franceschi, M., Frijia, G., Pini, G.A., 2021. The Mesozoic palaeoenvironmental richness of the Trieste Karst. Geological Field Trips 13 (2.2), 1–40. https://doi.org/10.3301/GFT.2021.06.
Cramer, B.D., Jarvis, I., 2020. Carbon isotope stratigraphy. Chapter 11 - Carbon Isotope Stratigraphy. In: Gradstein, Felix M., Ogg, James G., Schmitz, Mark D., Ogg, Gabi M. (Eds.), Geologic Time Scale 2020. Elsevier, pp. 309–343. https://doi.org/10.1016/B978-0-12-824360-2.00011-5, 2020.
Del Viscio, G., Morsilli, M., Posenato, R., Frijia, G., Moro, A., Mezga, A., 2022. Proliferation of Chondrodonta in upper Cenomanian shallow-water limestones of the Adriatic Carbonate Platform (Croatia) as a proxy of environmental instability. Cretaceous Research 134. https://doi.org/10.1016/j.cretres.2022.105151.
Dickson, J., Coleman, M., 1990. Changes in carbon and oxygen isotope composition during limestone diagenesis. In: Tucker, Maurice E., Bathurst, Robin G.C. (Eds.), Carbonate Diagenesis. Wiley, pp. 259–270. https://doi.org/10.1002/9781444304510.ch21.
Drzewiecki, P.A., Simo, J., 1997. Carbonate platform drowning and oceanic anoxic events on a mid-Cretaceous carbonate platform, south-central Pyrenees, Spain. Journal of Sedimentary Research 67 (4), 698–714.
Du Vivier, A.D., Jacobson, A.D., Lehn, G.O., Selby, D., Hurtgen, M.T., Sageman, B.B., 2015. Ca isotope stratigraphy across the Cenomanian–Turonian OAE 2: Links between volcanism, seawater geochemistry, and the carbonate fractionation factor. Earth and Planetary Science Letters 416, 121–131. https://doi.org/10.1016/j.epsl.2015.02.001.
Eaton, L.J., Stratto, G.W., Sanderson, K.R., 1996. Fertilizer phosphorus in lowbush blueberries: effects and fate. Acta Horticulturae 446, 477–486.
Einsele, G., Wiedmann, J., 1983. Cretaceous upwelling off northwest Africa: a summary. In: Coastal Upwelling, Its Sediment Record. Part B: Sedimentary Records of Ancient Coastal Upwelling. Plenum Press, New York, pp. 105–121.
Eldrett, J.S., Minisini, D., Bergman, S.C., 2014. Decoupling of the carbon cycle during Ocean Anoxic Event 2. Geology 42 (7), 567–570.
Erba, E., Bartolini, A., Larson, R.L., 2004. The Valanginian "Weissert Oceanic Anoxic Event". Geology 32, 149–152.
Erbacher, J., Thurow, J., Littke, R., 1996. Evolution patterns of radiolaria and organic matter variations: a new approach to identify sea-level changes in mid-Cretaceous pelagic environments. Geology 24 (6), 499–502.
Espitalié, J., Deroo, G., Marquis, F., 1985. La pyrolyse Rock-Eval et ses applications. Deuxième partie. Revue de l'Institut Français du Petrole 40 (6), 755–784.
Falzoni, F., Petrizzo, M.R., 2020. Patterns of planktonic foraminiferal extinctions and eclipses during Oceanic Anoxic Event 2 at Eastbourne (SE England) and other mid-low latitude locations. Cretaceous Research 116. https://doi.org/10.1016/j.cretres.2020.104593.
Forster, A., Schouten, S., Moriya, K., Wilson, P.A., Sinninghe Damsté, J.S., 2007. Tropical warming and intermittent cooling during the Cenomanian/Turonian oceanic anoxic event 2: Sea surface temperature records from the equatorial Atlantic. Paleoceanography 22 (1), 2006PA001349. https://doi.org/10.1029/2006PA001349.
Friedrich, O., Erbacher, J., Moriya, K., Wilson, P.A., Kuhnert, H., 2008. Warm saline intermediate waters in the Cretaceous Tropical Atlantic Ocean. Nature Geoscience 1 (7), 453–457.
Frijia, G., Parente, M., 2008. Strontium isotope stratigraphy in the upper Cenomanian shallow-water carbonates of the southern Apennines: Short-term perturbations of marine 87Sr/86Sr during the oceanic anoxic event 2. Palaeogeography, Palaeoclimatology, Palaeoecology 261, 15–29. https://doi.org/10.1016/j.palaeo.2008.01.003.URL.
Frijia, G., Parente, M., Di Lucia, M., Mutti, M., 2015. Carbon and strontium isotope stratigraphy of the Upper Cretaceous (Cenomanian-Campanian) shallow-water carbonates of southern Italy: Chronostratigraphic calibration of larger foraminifera biostratigraphy. Cretaceous Research 53, 110–139. https://doi.org/10.1016/j.cretres.2014.11.002.
Frijia, G., Forkner, R., Minisini, D., Pacton, M., Struck, U., Mutti, M., 2019. Cyanobacteria proliferation in the Cenomanian/Turonian boundary interval of the Apennine Carbonate Platform: immediate response to the environmental perturbations associated with OAE-2? Geochemistry, Geophysics, Geosystems 20 (6), 2698–2716. https://doi.org/10.1029/2019GC008306.
Gale, A.S., Christensen, W.K., 1996. Occurrence of the belemnite *Actinocamax plenus* in the Cenomanian of SE France and its significance. Bulletin of the Geological Society of Denmark 43 (1), 68–77.
Gangl, S., Moy, C., Stirling, C., Jenkyns, H., Crampton, J., Clarkson, M., Ohneiser, C., Porcelli, D., 2019. High-resolution records of Oceanic Anoxic Event 2: Insights into the timing, duration and extent of environmental perturbations from the palaeo-South Pacific Ocean. Earth and Planetary Science Letters 518, 172–182. https://doi.org/10.1016/j.epsl.2019.04.028.
Gertsch, B., Adatte, T., Keller, G., Tantawy, A.A.A., Berner, Z., Mort, H.P., Fleitmann, D., 2010. Middle and late Cenomanian oceanic anoxic events in shallow and deeper shelf environments of western Morocco. Sedimentology 57 (6), 1430–1462.
Grotzinger, J.P., Fike, D.A., Fischer, W.W., 2011. Enigmatic origin of the largest-known carbon isotope excursion in Earth's history. Nature Geoscience 4 (5), 285–292.
Handoh, I.C., Lenton, T.M., 2003. Periodic mid-Cretaceous oceanic anoxic events linked by oscillations of the phosphorus and oxygen biogeochemical cycles. Global Biogeochemical Cycles 17 (4).
Hardas, P., Mutterlose, J., 2007. Calcareous nannofossil assemblages of Oceanic Anoxic Event 2 in the equatorial Atlantic: Evidence of an eutrophication event. Marine Micropaleontology 66 (1), 52–69.
Hilbrecht, H., Frieg, C., Tröger, K.-A., Voigt, S., Voigt, T., 1996. Shallow water facies during the Cenomanian/Turonian anoxic event: bio-events, isotopes, and sea level in southern Germany. Cretaceous Research 17 (2), 229–253.
Huber, B.T., Norris, R.D., MacLeod, K.G., 2002. Deep-sea paleotemperature record of extreme warmth during the Cretaceous. Geology 30 (2), 123–126.
Huber, B.T., MacLeod, K.G., Watkins, D.K., Coffin, M.F., 2018. The rise and fall of the Cretaceous Hot Greenhouse climate. Global and Planetary Change 167, 1–23.
Hunt, J., 1995. Petroleum geochemistry and geology. Textbook, second ed. W. H. Freeman, New York, p. 743.
Immenhauser, A., Kenter, J.A., Ganssen, G., Bahamonde, J.R., Van Vliet, A., Saher, M.H., 2002. Origin and significance of isotope shifts in Pennsylvanian carbonates (Asturias, NW Spain). Journal of Sedimentary Research 72 (1), 82–94.
Immenhauser, A., Holmden, C., Patterson, W.P., 2008. Interpreting the carbon-isotope record of ancient shallow epeiric seas: lessons from the recent. Dynamics of Epeiric Seas 48, 137–174.
Jarvis, I., Mabrouk, A., Moody, R.T., de Cabrera, S., 2002. Late Cretaceous (Campanian) carbon isotope events, sea-level change and correlation of the Tethyan and Boreal realms. Palaeogeography, Palaeoclimatology, Palaeoecology 188 (3–4), 215–248.
Jarvis, I., Gale, A., Jenkyns, H., Pearce, M., 2006. Secular variation in Late Cretaceous carbon isotopes and sea-level change: evidence from a new $\delta^{13}C$ carbonate reference curve for the Cenomanian–Campanian (99.6–70.6 Ma). Geological Magazine 143 (5), 561–608.
Jarvis, I., Lignum, J.S., Gröcke, D.R., Jenkyns, H.C., Pearce, M.A., 2011. Black shale deposition, atmospheric CO_2 drawdown, and cooling during the Cenomanian/Turonian Oceanic Anoxic Event. Paleoceanography 26 (3), PA3201. https://doi.org/10.1029/2010PA002081.
Jenkyns, H.C., 1980. Cretaceous anoxic events: from continents to oceans. Journal of the Geological Society 137 (2), 171–188.
Jenkyns, H.C., 2010. Geochemistry of oceanic anoxic events: REVIEW. Geochemistry, Geophysics, Geosystems 11 (3), Q03004. https://doi.org/10.1029/2009GC002788.
Jenkyns, H.C., Dickson, A.J., Ruhl, M., Van Den Boorn, S.H.J.M., 2017. Basalt-seawater interaction, the Plenus Cold Event, enhanced weathering and geochemical change: deconstructing Oceanic Anoxic Event 2 (Cenomanian–Turonian, Late Cretaceous). Sedimentology 64 (1), 16–43. https://doi.org/10.1111/sed.12305.
Joachimski, M.M., 1994. Subaerial exposure and deposition of shallowing upward sequences: evidence from stable isotopes of Purbeckian peritidal carbonates (basal Cretaceous), Swiss and French Jura Mountains. Sedimentology 41 (4), 805–824.
Jones, C.E., Jenkyns, H.C., 2001. Seawater strontium isotopes, oceanic anoxic events, and seafloor hydrothermal activity in the Jurassic and Cretaceous. American Journal of Science 301 (2), 112–149.
Jurkovšek, B., Biolchi, S., Furlani, S., Kolar-Jurkovšek, T., Zini, L., Jež, J., Tunis, G., Bavec, M., Cucchi, F., 2016. Geology of the Classical Karst Region (SW Slovenia–NE Italy). Journal of Maps 12 (Suppl. 1), 352–362. https://doi.org/10.1080/17445647.2016.1215941.
Kerr, A.C., 1998. Oceanic plateau formation: a cause of mass extinction and black shale deposition around the Cenomanian–Turonian boundary? Journal of the Geological Society 155 (4), 619–626.
Khozyem, H., Adatte, T., Keller, G., Spangenberg, J.E., 2021. Organic carbon isotope records of the Paleocene- Eocene thermal maximum event in India provide new insights into mammal origination and migration. Journal of Asian Earth Sciences 212. https://doi.org/10.1016/j.jseaes.2021.104736.
Korbar, T., Glumac, B., Tesovic, B.C., Cadieux, S.B., 2012. Response of a carbonate platform to the Cenomanian/Turonian Drowning and OAE 2: a case study from the Adriatic Platform (Dalmatia, Croatia). Journal of Sedimentary Research 82 (3), 163–176. https://doi.org/10.2110/jsr.2012/17.
Kraal, P., Slomp, C.P., Forster, A., Kuypers, M.M., 2010. Phosphorus cycling from the margin to abyssal depths in the proto-Atlantic during oceanic anoxic event 2. Palaeogeography, Palaeoclimatology, Palaeoecology 295 (1–2), 42–54. https://doi.org/10.1016/j.palaeo.2010.05.014.
Krajewski, K.P., 2011. Phosphatic microbialites in the Triassic phosphogenic facies of Svalbard. Chapter Book "Interaction of Microbes with Sediments. Cellular Origin. In: Tewari, V., Seckbach, J. (Eds.), Life in Extreme Habitats and

Astrobiology, vol. 18. Springer, Dordrecht, pp. 187–222. https://doi.org/10.1007/978-94-007-0397-1_9.
Kuypers, M.M., Pancost, R.D., Nijenhuis, I.A., Sinninghe Damsté, J.S., 2002. Enhanced productivity led to increased organic carbon burial in the euxinic North Atlantic basin during the late Cenomanian oceanic anoxic event. Paleoceanography 17 (4), 3–1.
Křížová, B., Consorti, L., Cardelli, S., Schmitt, K., Brombin, V., Franceschi, M., Tunis, G., Bonini, L., Frijia, G., 2024. Late Cretaceous (Cenomanian- Turonian) temperature evolution and biotic response in the Adriatic Carbonate Platform region of Friuli, northeast Italy. Palaeogeography, Palaeoclimatology, Palaeoecology 637. https://doi.org/10.1016/j.palaeo.2023.111995.
Larson, R.L., 1991. Geological consequences of superplumes. Geology 19 (10), 963–966.
Larson, R.L., Erba, E., 1999. Onset of the Mid-Cretaceous greenhouse in the Barremian-Aptian: Igneous events and the biological, sedimentary, and geochemical responses. Paleoceanography 14 (6), 663–678.
Manabe, S., Bryan Jr, K., 1985. CO2-induced change in a coupled ocean-atmosphere model and its paleoclimatic implications. Journal of Geophysical Research: Oceans 90 (C6), 11689–11707.
Marshall, J.D., 1992. Climatic and oceanographic isotopic signals from the carbonate rock record and their preservation. Geological Magazine 129 (2), 143–160.
Mort, H., Jacquat, O., Adatte, T., Steinmann, P., Föllmi, K., Matera, V., Berner, Z., Stüben, D., 2007. The Cenomanian/Turonian anoxic event at the Bonarelli Level in Italy and Spain: enhanced productivity and/or better preservation? Cretaceous Research 28 (4), 597–612. https://doi.org/10.1016/j.cretres.2006.09.003.
Mort, H.P., Adatte, T., Keller, G., Bartels, D., Föllmi, K.B., Steinmann, P., Berner, Z., Chellai, E., 2008. Organic carbon deposition and phosphorus accumulation during Oceanic Anoxic Event 2 in Tarfaya, Morocco. Cretaceous Research 29 (5–6), 1008–1023. https://doi.org/10.1016/j.cretres.2008.05.026.
Navarro-Ramirez, J., Bodin, S., Consorti, L., Immenhauser, A., 2017. Response of western South American epeiric-neritic ecosystem to middle Cretaceous Oceanic Anoxic Events. Cretaceous Research 75, 61–80.
O'Brien, C.L., Robinson, S.A., Pancost, R.D., Damsté, J.S.S., Schouten, S., Lunt, D.J., Alsenz, H., Bornemann, A., Bottini, C., Brassell, S.C., et al., 2017. Cretaceous sea-surface temperature evolution: Constraints from TEX86 and planktonic foraminiferal oxygen isotopes. Earth-Science Reviews 172, 224–247.
O'Connor, L.K., Jenkyns, H.C., Robinson, S.A., Remmelzwaal, S.R.C., Batenburg, S.J., Parkinson, I.J., Gale, A.S., 2020. A Re-evaluation of the Plenus Cold Event, and the Links Between CO_2, Temperature, and Sea-water Chemistry During OAE 2. Paleoceanography and Paleoclimatology 35 (4). https://doi.org/10.1029/2019PA003631.
Owen-Smith, T., Ashwal, L., Sudo, M., Trumbull, R.B., 2017. Age and petrogenesis of the Doros Complex, Namibia, and implications for early plume-derived melts in the Paraná–Etendeka LIP. Journal of Petrology 58 (3), 423–442.
Owens, J.D., Gill, B.C., Jenkyns, H.C., Bates, S.M., Severmann, S., Kuypers, M.M., Woodfine, R.G., Lyons, T.W., 2013. Sulfur isotopes track the global extent and dynamics of euxinia during Cretaceous Oceanic Anoxic Event 2. Proceedings of the National Academy of Sciences 110 (46), 18407–18412. https://doi.org/10.1073/pnas.1305304110.
Parente, M., Frijia, G., Di Lucia, M., 2007. Carbon-isotope stratigraphy of Cenomanian–Turonian platform carbonates from the southern Apennines (Italy): a chemostratigraphic approach to the problem of correlation between shallow-water and deep-water successions. Journal of the Geological Society 164 (3), 609–620. https://doi.org/10.1144/0016-76492006-010.
Parente, M., Frijia, G., Di Lucia, M., Jenkyns, H.C., Woodfine, R.G., Baroncini, F., 2008. Stepwise extinction of larger foraminifera at the Cenomanian- Turonian boundary: A shallow-water perspective on nutrient fluctuations during Oceanic Anoxic Event 2 (Bonarelli Event). Geology 36 (9). https://doi.org/10.1130/G24893A.1.
Parrish, J.T., Curtis, R.L., 1982. Atmospheric circulation, upwelling, and organic-rich rocks in the Mesozoic and Cenozoic eras. Palaeogeography, Palaeoclimatology, Palaeoecology 40 (1–3), 31–66.
Patacca, E., Scandone, P., 2007. Geology of the southern Apennines. Bollettino della Societa Geologica Italiana 7, 75–119.
Paul, C., Lamolda, M., Mitchell, S., Vaziri, M., Gorostidi, A., Marshall, J., 1999. The Cenomanian–Turonian boundary at Eastbourne (Sussex, UK): a proposed European reference section. Palaeogeography, Palaeoclimatology, Palaeoecology 150 (1–2), 83–121. https://doi.org/10.1016/S0031-0182(99)00009-7.
Percival, L., Witt, M., Mather, T., Hermoso, M., Jenkyns, H., Hesselbo, S., Al-Suwaidi, A., Storm, M., Xu, W., Ruhl, M., 2015. Globally enhanced mercury deposition during the end-Pliensbachian extinction and Toarcian OAE: A link to the Karoo–Ferrar Large Igneous Province. Earth and Planetary Science Letters 428, 267–280. https://doi.org/10.1016/j.epsl.2015.06.064.
Petrizzo, M.R., Parente, M., Falzoni, F., Bottini, C., Frijia, G., Steuber, T., Erba, E., 2025. Calcareous plankton and shallow-water benthic biocalcifiers: Resilience and extinction across the Cenomanian-Turonian Oceanic Anoxic Event 2. Palaeogeography, Palaeoclimatology, Palaeoecology, 112891. https://doi.org/10.1016/j.palaeo.2025.112891.
Philip, J.M., Airaud-Crumiere, C., 1991. The demise of the rudist-bearing carbonate platforms at the Cenomanian/Turonian boundary: a global control. Coral Reefs 10 (2), 115–125.
Picotti, V., Cobianchi, M., 2017. Jurassic stratigraphy of the Belluno Basin and Friuli Platform: a perspective on far-field compression in the Adria passive margin. Swiss Journal of Geosciences 110 (3), 833–850.
Picotti, V., Cobianchi, M., Luciani, V., Blattmann, F., Schenker, T., Mariani, E., Bernasconi, S.M., Weissert, H., 2019. Change from rimmed to ramp platform forced by regional and global events in the Cretaceous of the Friuli-Adriatic Platform (Southern Alps, Italy). Cretaceous Research 104. https://doi.org/10.1016/j.cretres.2019.07.007.
Pogge von Strandmann, P.A.E., Jenkyns, H.C., Woodfine, R.G., 2013. Lithium isotope evidence for enhanced weathering during Oceanic Anoxic Event 2. Nature Geoscience 6 (8), 668–672. https://doi.org/10.1038/ngeo1875. 1752-0908.
Posenato, R., Frijia, G., Morsilli, M., Moro, A., Del Viscio, G., Mezga, A., 2020. Paleoecology and proliferation of the bivalve Chondrodonta joannae (Choffat) in the upper Cenomanian (Upper Cretaceous) Adriatic Carbonate Platform of Istria (Croatia). Palaeogeography, Palaeoclimatology, Palaeoecology 548. https://doi.org/10.1016/j.palaeo.2020.109703.
Poulsen, C.J., Barron, E.J., Arthur, M.A., Peterson, W.H., 2001. Response of the mid-Cretaceous global oceanic circulation to tectonic and CO2 forcings. Paleoceanography 16 (6), 576–592.
Schlagintweit, F., Yazdi-Moghadam, M., 2022. What's in a name? Revision of Peneroplis turonicus Said and Kenawy, 1957 (benthic foraminifera), an inappropriately-named taxon from the Cenomanian of the southern Neotethys margin. Revue de Micropaleontologie 75, 100612.
Schlanger, S., Jenkyns, H., 1976. Cretaceous oceanic anoxic events: causes and consequences. Geologie en Mijnbouw 55 (3–4).
Scholle, P.A., Arthur, M.A., 1980. Carbon isotope fluctuations in Cretaceous pelagic limestones: potential stratigraphic and petroleum exploration tool. AAPG Bulletin 64 (1), 67–87.
Seton, M., Gaina, C., Müller, R., Heine, C., 2009. Mid-Cretaceous seafloor spreading pulse: Fact or fiction? Geology 37 (8), 687–690.
Sinton, C., Duncan, R., 1997. Potential links between ocean plateau volcanism and global ocean anoxia at the Cenomanian/Turonian boundary. Economic Geology 92 (7–8), 836–842.
Snow, L.J., Duncan, R.A., Bralower, T.J., 2005. Trace element abundances in the Rock Canyon Anticline, Pueblo, Colorado, marine sedimentary section and their relationship to Caribbean plateau construction and oxygen anoxic event 2. Paleoceanography 20 (3). https://doi.org/10.1029/2004PA001093.
Steuber, T., Rauch, M., Masse, J.-P., Graaf, J., Malkoč, M., 2005. Low-latitude seasonality of Cretaceous temperatures in warm and cold episodes. Nature 437 (7063), 1341–1344.
Steuber, T., Löser, H., Mutterlose, J., Parente, M., 2023. Biogeodynamics of Cretaceous marine carbonate production. Earth-Science Reviews 238. https://doi.org/10.1016/j.earscirev.2023.104341.
Swart, P.K., Oehlert, A.M., 2018. Revised interpretations of stable C and O patterns in carbonate rocks resulting from meteoric diagenesis. Sedimentary Geology 364, 14–23.
Sweere, T.C., Dickson, A.J., Jenkyns, H.C., Porcelli, D., Elrick, M., van den Boorn, S.H., Henderson, G.M., 2018. Isotopic evidence for changes in the zinc cycle during Oceanic Anoxic Event 2 (Late Cretaceous). Geology 46 (5), 463–466. https://doi.org/10.1130/G40226.
Takashima, R., Gautam, P., Nishi, H., 2006. Recent advances in research on terrestrial and marine sequences from the Mid-Cretaceous Oceanic Anoxic Events (OAEs). Scientific Drilling 2, 50–51. https://doi.org/10.5194/sd-2-50-2006.
Tsandev, I., Slomp, C., 2009. Modeling phosphorus cycling and carbon burial during Cretaceous Oceanic Anoxic Events. Earth and Planetary Science Letters 286 (1–2), 71–79.
Tsikos, H., Jenkyns, H., Walsworth-Bell, B., Petrizzo, M., Forster, A., Kolonic, S., Erba, E., Premoli Silva, I., Baas, M., Wagner, T., Sinninghe Damsté, J., 2004. Carbon-isotope stratigraphy recorded by the Cenomanian–Turonian Oceanic Anoxic Event: correlation and implications based on three key localities. Journal of the Geological Society 161 (4), 711–719. https://doi.org/10.1144/0016-764903-077.
Turgeon, S.C., Creaser, R.A., 2008. Cretaceous oceanic anoxic event 2 triggered by a massive magmatic episode. Nature 454 (7202), 323–326.
Van Cappellen, P., Ingall, E.D., 1994. Benthic phosphorus regeneration, net primary production, and ocean anoxia: A model of the coupled marine biogeochemical cycles of carbon and phosphorus. Paleoceanography 9 (5), 677–692.
Veizer, J., Prokoph, A., 2015. Temperatures and oxygen isotopic composition of Phanerozoic oceans. Earth-Science Reviews 146, 92–104. https://doi.org/10.1016/j.earscirev.2015.03.008.
Vlahović, I., Tišljar, J., Velić, I., Matičec, D., 2005. Evolution of the Adriatic Carbonate Platform: Palaeogeography, main events and depositional dynamics. Palaeogeography, Palaeoclimatology, Palaeoecology 220 (3–4), 333–360. https://doi.org/10.1016/j.palaeo.2005.01.011.
Voigt, S., Gale, A.S., Voigt, T., 2006. Sea-level change, carbon cycling and palaeoclimate during the Late Cenomanian of northwest Europe; an integrated palaeoenvironmental analysis. Cretaceous Research 27 (6), 836–858. https://doi.org/10.1016/j.cretres.2006.04.005.
Wagner, T., Wallmann, K., Herrle, J.O., Hofmann, P., Stuesser, I., 2007. Consequences of moderate 25,000 yr lasting emission of light CO2 into the mid-Cretaceous ocean. Earth and Planetary Science Letters 259 (1–2), 200–211.
Weissert, H., McKenzie, J., Channell, J., 1985. Natural variations in the carbon cycle during the Early Cretaceous. In: Sundquist, E.T., Broecker, W.S. (Eds.), The carbon cycle and atmospheric CO2: natural variations Archean to Present, pp. 531–545. https://doi.org/10.1029/GM032.

Westermann, S., Caron, M., Fiet, N., Fleitmann, D., Matera, V., Adatte, T., Föllmi, K.B., 2010. Evidence for oxic conditions during oceanic anoxic event 2 in the northern Tethyan pelagic realm. Cretaceous Research 31 (5), 500–514. https://doi.org/10.1016/j.cretres.2010.07.001.

Zheng, X.Y., Jenkyns, H.C., Gale, A.S., Ward, D.J., Henderson, G.M., 2013. Changing ocean circulation and hydrothermal inputs during Ocean Anoxic Event 2 (Cenomanian–Turonian): evidence from Nd-isotopes in the European shelf sea. Earth and Planetary Science Letters 375, 338–348.

Zhou, X., Jenkyns, H.C., Owens, J.D., Junium, C.K., Zheng, X.-Y., Sageman, B.B., Hardisty, D.S., Lyons, T.W., Ridgwell, A., Lu, Z., 2015. Upper ocean oxygenation dynamics from I/Ca ratios during the Cenomanian/Turonian OAE 2. Paleoceanography 30 (5), 510–526.

List of taxa

Cyanobacteria
Decastronema Golubić, Radoičić & S.-J. Lee, 2008
Microproblematica
Thaumatoporella Pia, 1927
Foraminifera
Cuneolina d'Orbigny, 1839
Discorbidae Ehrenberg, 1838
Miliolidae Ehrenberg, 1838
Neodubrovnikella turonica (Said & Kenawi, 1957)
Rotorbinella mesogeensis (Tronchetti)
Rotorbinella Bandy, 1944
Nezzazata Omara, 1956
Scandonea De Castro, 1971
Siphopfenderina Schlagintweit & Septfontaine, 2023
Spiroplectammina multicamerata Said & Kenawy, 1957
Bivalves
Chondrodonta Stanton, 1901

Appendix A. Supplementary data

Supplementary data to this article can be found online at https://doi.org/10.1016/j.cretres.2025.106133.